



# Modeled Greenland Ice Sheet evolution constrained by ice-core-derived Holocene elevation histories

Mikkel L. Lauritzen<sup>1</sup>, Anne Solgaard<sup>3</sup>, Nicholas Rathmann<sup>1</sup>, Bo M. Vinther<sup>1</sup>, Aslak Grindsted<sup>1</sup>, Brice Noël<sup>4</sup>, Guðfinna Aðalgeirsdóttir<sup>2</sup>, and Christine S. Hvidberg<sup>1</sup>

<sup>1</sup>Niels Bohr Institute, University of Copenhagen, Copenhagen, Denmark

<sup>2</sup>Institute of Earth Sciences, University of Iceland, Reykjavík, Iceland

<sup>3</sup>Geological Survey of Denmark and Greenland, Copenhagen, Denmark

<sup>4</sup>Department of Geography Laboratoire de Climatologie et Topoclimatologie, University of Liège, Liège, Belgium

**Correspondence:** Mikkel L. Lauritzen (mikkel.lauritzen@nbi.ku.dk)

**Abstract.** During the Holocene, the Greenland Ice Sheet (GrIS) experienced substantial thinning, with some regions losing up to 600 meters of ice. Ice sheet reconstructions, paleoclimatic records, and geological evidence indicate that during the Last Glacial Maximum, the GrIS extended far beyond its current boundaries and was connected with the Innuitian Ice Sheet (IIS) in the northwest. We investigate these long-term geometry changes and explore several possible factors driving those changes by using the Parallel Ice Sheet Model (PISM) to simulate the GrIS thinning throughout the Holocene period, from 11.7 ka ago to the present. We perform an ensemble study of 841 model simulations in which key model parameters are systematically varied to determine the parameter values that, with quantified uncertainties, best reproduce the 11.7 ka of surface elevation records derived from ice cores, providing confidence in the modeled GrIS historical evolution. We find that since the Holocene onset, 11.7 ka ago, the GrIS mass loss has contributed  $5.3 \pm 0.3$  m to the mean global sea level rise, which is consistent with the ice-core-derived thinning curves spanning the time when the GrIS and the Innuitian Ice Sheet were bridged. Our results suggest that the ice bridge collapsed  $4.9 \pm 0.5$  ka ago and that the GrIS is still responding to these past changes today, having raised sea level by  $23 \pm 26$  mm SLE  $\text{ka}^{-1}$  in the last 500 years. Our results have implications for future mass-loss projections, which should account for this long-term, transient trend.

## 1 Introduction

During the Last Glacial Maximum (LGM), approximately 20 ka ago, Earth was covered by large ice sheets, including the Laurentide, the Fenno-Scandian, the Innuitian, and the Greenlandic ice sheets, and the global mean sea level was 125–134 m lower than it is today (Gulev et al., 2021). Geological evidence suggests that the Greenland Ice Sheet (GrIS) extended to the continental shelf and was connected to the Innuitian Ice Sheet (IIS) at the Nares Strait (England et al., 2006).

Towards the end of the last glacial period, the Bølling-Allerød interstadial brought an abrupt warming to the Northern Hemisphere 14.7 ka ago, followed by the cooling of the Younger Dryas stadial 12.9 ka ago (Rasmussen et al., 2006). The Holocene warm interglacial began 11.7 ka ago, bringing temperatures that were locally up to 15°C warmer in Greenland (Andersen et al., 2004). However, temperature reconstructions vary by several degrees, which can significantly affect the



modeled GrIS history (Nielsen et al., 2018). Following the Holocene Thermal Maximum, 8-5 ka ago, Greenland temperatures have shown a long-term decreasing trend (Vinther et al., 2009), but anthropogenic forcing has since reversed the course of natural temperature change, resulting in a global increase in temperatures since pre-industrial times (Eyring et al., 2021).

Accurately modeling the historical evolution of the GrIS is essential for evaluating and calibrating ice sheet models. Ice sheet models respond to climate change over a range of different timescales and are rarely in the steady state (e.g. Lauritzen et al., 2023). However, several ice sheet model studies have overlooked a calibration of their temporal evolution and only focused on the evolution of ice temperature, neglecting other delayed responses, such as bedrock dynamics. For example, the ISMIP6 protocol does not require any calibration (Nowicki et al., 2020), and it has been shown that the majority of the ISMIP6 ensemble simulations underestimate the observed IMBIE consensus mass loss from the Greenland Ice Sheet (The IMBIE Team, 2020; Aschwanden et al., 2021). Recent advances have made up for this by calibrating an ice sheet model to satellite-based gravimetry-derived mass loss data of the GrIS (Aschwanden and Brinkerhoff, 2022), but the satellite-based calibration data period only covers 22 years at the time of writing, and there is no guarantee that it gives a sensible long term response.

Calibrating the model to align with present-day observations of ice thickness and velocities risks capturing only the present-day state while being on a wrong state trajectory; that is, neglecting the long-term memory of the ice sheet and the response of the bedrock to past changes in ice load. These differences in past trajectories affect the projected future mass loss in this century as demonstrated by (Aðalgeirsdóttir et al., 2014). Beyond the satellite era and back to the early Holocene, no direct observations are available to inform on the ice sheet history, and ice sheet modeling must rely on proxy data from paleo-climatic records for constraining and validating the long-term transient response of the ice sheet (state trajectory) over these considerably longer timescales. Surface elevation histories, derived from deep ice cores at Camp Century (CC), NGRIP, GRIP, and Dye 3 (See Fig. 1), provide such constraints for modeling the GrIS through the Holocene (Vinther et al., 2009). These archives offer valuable insights into the ice sheet's dynamics through the past climate and significantly enhance the robustness of model predictions. Previous attempts to model the ice-core-derived elevation history have not been entirely successful, most likely because the studies did not include the dynamic effect from the IIS on the GrIS in the early Holocene. (Lecavalier et al., 2013, 2017).

In this study, we use the Parallel Ice Sheet Model (PISM) to model the GrIS and the collapse of the IIS bridge during the Holocene. By varying 20 key model parameters in an 841 ensemble-member study, we show that it is possible to model the ice-core-derived elevation histories *if* the grounding line is allowed to advance to the continental shelf *and* the modeled GrIS can form a connection to the IIS. We use this setup to constrain the model parameters for the ensemble and to estimate the GrIS temporal evolution with quantified uncertainties. Using the calibrated model, we investigate the ice sheet mass loss throughout the Holocene and determine the current long-term response of the modeled GrIS and bedrock dynamics.

## 2 Paleoclimatic evidence

When water evaporates over the oceans and precipitates over the GrIS, a fractionation process changes the ratio between the oxygen isotopes in the water. This process is temperature dependent, which was first used by Dansgaard et al. (1969) to infer past temperatures from measurements of oxygen isotopes at CC. The temperatures over the GrIS change locally both because



of regional temperature changes and due to surface elevation changes. Vinther et al. (2009) were able to derive a GrIS-wide temperature signal by assuming that the Renland and Aggasiz ice core sites are located within restricted ice domes such that the ice thickness does not change. This GrIS-wide temperature signal was then subtracted from the oxygen isotope signals at CC, NGRIP, GRIP, and Dye 3 to derive local surface elevation histories, having adjusted from upstream effects.

60 We use five different ice-core-based temperature anomaly reconstructions described by Nielsen et al. (2018) to account for the uncertainty in the past temperatures. The temperature reconstructions are shown in Fig. A1. Reconstruction number 1 and 2 are based on the GRIP ice core using a linear transfer function from Huybrechts (2002) and quadratic transfer function from Johnsen et al. (1995), reconstruction number 3 is based on the NGRIP ice core again using the transfer function from Huybrechts (2002), reconstruction number 4 is the GrIS-wide reconstruction from Vinther et al. (2009). Reconstruction number 65 5 is based on the NGRIP core using an inversion scheme for the isotope diffusion (Gkinis et al., 2014). Reconstruction number 1 is the reconstruction used by the SeaRISE project (Bindschadler et al., 2013). The Holocene climate in Greenland is relatively stable and started with an abrupt warming of approximately 15°C at the glacial-interglacial transition 11.7 ka ago, followed by the Holocene Thermal Maximum ~8-5 ka ago with temperatures 2-3°C higher than the 20th century mean, and then a general cooling trend until the late 20th century. The Holocene Thermal Maximum is only captured by reconstructions numbers 3, 4, 70 and 5, while reconstructions 1 and 2 suggest a constant Holocene climate.

### 3 Model setup

To model the Holocene evolution of the GrIS, we use the open-source Parallel Ice Sheet Model (PISM) version 2.1 (Bueler and Brown, 2009; Winkelmann et al., 2011). PISM is a three-dimensional thermomechanically-coupled ice sheet model that solves 75 non-sliding, shearing flow in the slow-moving interior of the GrIS and fast membrane-stress-type flow, sliding over the base in the fast flowing ice streams and outlet glaciers. At the ice-ocean boundary, PISM incorporates sub-grid parameterizations to robustly model grounding line advance and retreat (Gladstone et al., 2010). Model parameters that are introduced in this section will be varied in our ensemble of simulations using the ranges listed in Table 1 unless otherwise specified.

#### 3.1 Model domain

80 The model domain is shown in Fig. 1 and extends from the continental shelf in the east to the Canadian Arctic Archipelago in the west, covering an area of  $6.7 \times 10^6$  km<sup>2</sup>. A north polar stereographic projection is used with a standard parallel latitude of 70° N and a central longitude of -45° W corresponding to ESPG 3413. The area is distorted by a maximum of +5% in the north and -11% in the southwest compared to the central longitude and latitude. PISM uses a flat earth approximation and volume is thus not conserved when transforming thickness between projections. All estimated volumes and mass loss rates are given by 85 accounting for the actual grid area.

To allow for a meaningful partitioning of mass between Greenland and Canada, we introduce an Extended Continental Shelf (ECS) mask, which is equal to the Exclusive Economic Zone of Greenland (Flanders Marine Institute (VLIZ), Belgium, 2023).

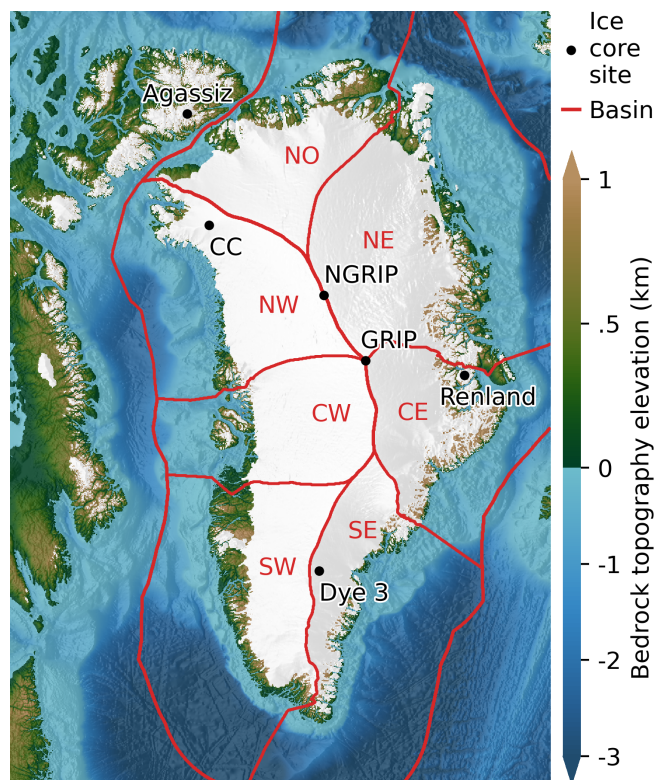


**Figure 1.** Model domain showing the present-day bedrock topography elevation from Morlighem (2022), Jakobsson et al. (2020), and GEBCO Bathymetric Compilation Group (2023) and the present-day ice cover from Morlighem (2022) and RGI Consortium (2023) shown in white. The ice core sites discussed in the text (CC, NGRIP, GRIP, Dye 3, Renland, and Agassiz) are shown on top together with the glacier catchment basins (NW, CW, SW, SE, CE, NE, NO) from Mouginot and Rignot (2019) and extended out to the Exclusive Economic Zone of Greenland (Flanders Marine Institute (VLIZ), Belgium, 2023) and constitute our extended continental shelf (ECS) domain, see text.

This divides Greenland and Canada at the Nares Strait and Baffin Bay while extending to the continental shelf in the north, east, and south. To also partition the mass loss within the GrIS when the grounding line advances beyond present-day positions, we extend the basins from Mouginot and Rignot (2019) to the ECS by nearest neighbor extrapolation.

The present-day bedrock topography over Greenland is from BedMachine v5 (Morlighem, 2022), and extended with IBCAO v4.2 (Jakobsson et al., 2020) and GEBCO Bathymetric Compilation Group (2023) to cover the larger domain, in that order of preference to get the best bedrock available.

At the lateral boundary, a Dirichlet boundary condition of zero ice thickness is used, and the influence of the majority of the Laurentide Ice Sheet is thereby neglected. The north and south are bounded by the open ocean, while Iceland and Svalbard are just visible towards the east. At the base of a 2 km deep bedrock thermal layer, the thermal heat flux from Shapiro (2004) is applied constantly in time.



### 3.2 Surface mass balance

Determining the surface mass balance (SMB) of the GrIS is challenging, and regional climate models (RCMs), such as  
100 RACMO, not only simulate the atmospheric conditions over the GrIS but also incorporate a detailed snowpack model to  
simulate precipitation, melt, percolation, refreezing, and sublimation processes (Noël et al., 2019).

Given the complexity of including all these processes, it is not feasible to run the RCM over thousands of years, as needed in  
our study, and we instead apply a Positive Degree Day (PDD) scheme to calculate the surface melting. This approach bases the  
SMB solely on temperature,  $T$ , and precipitation,  $P$ . In the PDD scheme, surface melt is proportional to the extent to which  
105 the temperature exceeds the freezing point (e.g. Braithwaite, 1985). We use two constants of proportionality: one for snow,  $\psi_s$ ,  
and another for ice,  $\psi_i$ .

To force the PDD model, we use a 12-month reference climatology based on the multi-year monthly averages of temperature  
and precipitation for the period 1960–1989 from the RACMO RCM. Since our model domain is not covered by a single  
RACMO simulation, we combine different simulations (see Fig. A3). We looked at three areas for rainfall data: Greenland,  
110 the Northern Canadian Arctic Archipelago, and the Southern Canadian Arctic Archipelago (Noël et al., 2018), treating areas  
outside these regions as having no rainfall. For temperature, we used RACMO2.3p2 at 5.5 km for Greenland (Noël et al., 2019)  
and combined it with a broader 11 km simulation (Noël et al., 2015) for the rest of the area. The mean precipitation and summer  
temperatures from the resulting climatology are shown in Fig. A2.

We account for historical temperature changes using the same domain-wide anomalies as in Nielsen et al. (2018), i.e., by  
115 adding a domain-wide, spatially uniform temperature anomaly,  $\Delta T$ , that varies in time, and a lapse rate adjustment,  $\Gamma$ , of  
the surface temperature relative to the RCM surface topography. Since the vapor pressure approximately scales exponentially  
with temperature in the Clausius-Clapeyron relation, we account for historical precipitation changes by scaling the reference  
precipitation field with a time-dependent scaling factor  $\exp(\omega(\phi)\Delta T(t))$ . Here,  $\omega$  has the latitude dependence

$$\omega(\phi(x, y)) = \begin{cases} \omega_{\downarrow} & \phi \leq \phi_{\downarrow} \\ \omega_{\downarrow} + \frac{\phi - \phi_{\downarrow}}{\phi_{\uparrow} - \phi_{\downarrow}}(\omega_{\uparrow} - \omega_{\downarrow}) & \phi_{\downarrow} \leq \phi \leq \phi_{\uparrow} \\ \omega_{\uparrow} & \phi_{\uparrow} \leq \phi \end{cases}, \quad (1)$$

120 where  $\phi$  is the latitude and  $\phi_{\downarrow} = 60^{\circ}N$  and  $\phi_{\uparrow} = 75^{\circ}N$ . In this way, we allow for different precipitation histories in Northern  
and Southern Greenland, unlike the uniform scaling used by many previous modeling attempts (e.g. Nielsen et al., 2018).

### 3.3 Ocean forcing

Following Aschwanden et al. (2019) we take the sub-shelf ocean melt to be separable in space and time

$$\dot{m}(x, y, t) = \dot{m}_x(\phi(x, y))\dot{m}_t(t), \quad (2)$$



125 with the spatial dependence controlling the present-day melt rate given by

$$\dot{m}_x(\phi(x, y)) = \begin{cases} \dot{m}_\downarrow & \phi \leq \phi_\downarrow \\ \dot{m}_\downarrow + \frac{\phi - \phi_\downarrow}{\phi_\uparrow - \phi_\downarrow} (\dot{m}_\uparrow - \dot{m}_\downarrow) & \phi_\downarrow \leq \phi \leq \phi_\uparrow, \\ \dot{m}_\uparrow & \phi_\uparrow \leq \phi \end{cases} \quad (3)$$

where  $\phi_\downarrow = 71^\circ N$  and  $\phi_\uparrow = 80^\circ N$  while  $\dot{m}_\downarrow$  and  $\dot{m}_\uparrow$  are the upper and lower melt values which we will vary. To allow the formation of an ice bridge to Canada, the sub-shelf melt rate is scaled by

$$\dot{m}_t(t) = \begin{cases} 0 & t \leq \tau \\ \frac{t - \tau}{\Delta\tau} & \tau \leq t \leq \tau + \Delta\tau, \\ 1 & \tau + \Delta\tau \leq t \end{cases} \quad (4)$$

130 such that there will be no ocean melt for times earlier than  $\tau$ , while it increases to present-day values in the time  $\Delta\tau$  inspired by the rapid change in ocean temperatures found by Clark et al. (2020). In addition to sub-surface melt, ice is calved off at the oceanfront at a rate that is proportional to the tensile von Mises stress and inversely proportional to a characteristic parameter,  $\sigma_{\max}$  (Morlighem et al., 2016). Additionally, all ice thinner than  $H_{cr}$  is calved off, and a eustatic sea level forcing from Imbrie and McIntyre (2006) is applied, changing the ocean level by 130 m in the last 19 ka.

### 135 3.4 Ice dynamics

The constitutive relation that relates the strain rate,  $\dot{\epsilon}_{ij}$ , to the stress,  $\tau_{ij}$ , in the ice sheet is

$$\dot{\epsilon}_{ij} = EA\tau_e^{n-1}\tau_{ij}, \quad (5)$$

where  $E$  is the enhancement factor,  $\tau_e$  is the effective deviatoric stress,  $n$  is the creep exponent, and  $A$  is the ice softness which depends on temperature, pressure, and water content of the ice. The enhancement factor and the creep exponents are taken to

140 be different for the SIA and the SSA, and we use  $E_{SSA} = 1.3, n_{SIA} = 3$  while we vary  $E_{SIA}$  and  $n_{SSA}$ . The basal sliding velocity  $\mathbf{u}_b$  in the SSA is related to the basal shear stress  $\tau_b$  through the pseudo-plastic power law:

$$\tau_b = -\tan(\phi)N_{\text{till}} \frac{\mathbf{u}_b}{u_{\text{th}}^q |\mathbf{u}_b|^{1-q}}, \quad (6)$$

where  $q$  is the sliding exponent,  $u_{\text{th}} = 100 \text{ m a}^{-1}$  is a characteristic speed. The till friction angle,  $\phi$ , is parameterized as a continuous function of bedrock topography that increases linearly from  $\phi_{\min}$  to  $\phi_{\max}$  between  $z_{\min}$  and  $z_{\max}$ . The effective

145 pressure on the till  $N_{\text{till}}$  depends on the water level in the till,  $W_{\text{till}}$ , and the overburden pressure of the ice,  $P_0$ :

$$N_{\text{till}} = \min \left\{ P_0, \tilde{N}_0 \left( \frac{\delta P_0}{\tilde{N}_0} \right)^{W_{\text{till}}/W_{\text{till}}^{\max}} \right\}, \quad (7)$$

where  $W_{\text{till}}^{\max} = 2 \text{ m}$  is the maximal water level in the till and  $\tilde{N}_0 = 5.6 \times 10^8 \text{ Pa}$  is a reference pressure simplified from the original formulation of Bueler and van Pelt (2015) to include the dependence of the till compressibility and the till void ratio.  $\delta$  controls the lower bound of the effective pressure, which we will vary in our simulations.

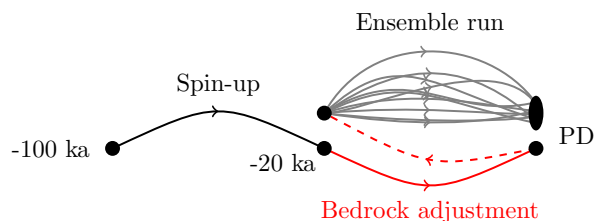


**Figure 2.** Schematic of the model ensemble experiment. The ice sheet is initialized at -100 ka using present-day geometry and run through the last glacial at 20 km resolution. The bedrock is then iteratively updated at -20 ka to reduce the modeled present-day bedrock topography deviation. After finding a suitable bedrock topography, the ice sheet model is branched off at -20 ka, and an ensemble of simulations is run at 10 km resolution.

### 150 3.5 Earth deformation and initialization

The bedrock responds to changes in ice load by the visco-elastic bed deformation model by Lingle and Clark (1985) and Bueler et al. (2007) with flexural rigidity  $D = 5 \times 10^{24}$  N m and upper mantle viscosity  $\eta = 1 \times 10^{21}$  Pa s.

We initialize the GrIS by running the model from -100 ka to -20 ka (all times are relative to 2 ka CE) at 20 km grid resolution with initial bedrock topography taken to be the same as the present day (Morlighem, 2022; Jakobsson et al., 2020; GEBCO  
155 Bathymetric Compilation Group, 2023). To get a modeled bedrock topography at the end of the simulations as close to the observed present-day bedrock topography as possible we iteratively adjust the bedrock at -20 ka as depicted in Fig. 2. A simulation in 20 km resolution is run from -20 ka to present day, after which the modeled bedrock deviation from the observed is used to update the bedrock at -20 ka according to

$$b_{i+1}^0 = b_i^0 + K(b^{\text{obs}} - b_i^1), \quad (8)$$

160 where  $b^{\text{obs}}$  is the observed present-day topography (Morlighem, 2022; Jakobsson et al., 2020; GEBCO Bathymetric Compilation Group, 2023),  $b_i^0$  is the modeled bedrock topography at -20 ka and  $b_i^1$  is the modeled bedrock topography at present day. The relaxation parameter  $K = 0.7$  is used to prevent overcompensation that leads to unwanted deglaciation. Using this method, the RMSE of the bedrock went from 77.4 m to 3.3 m after 20 iterations, as shown in Fig. 3.

At -20 ka, the run is branched using the best  $b^0$  from the bedrock adjustment, and an ensemble of simulations is run at 10  
165 km grid resolution until the present day, varying the 20 key parameters listed in Table 1.

## 4 Bayesian inference

To account for model uncertainty and determine the importance of the model parameters, we run an ensemble of simulations from -20 ka to present day, varying the 20 parameters listed in Table 1. The 20 parameters share the same dynamical parameters as those varied by Aschwanden and Brinkerhoff (2022), while the oceanic and atmospheric parameters chosen reflect the

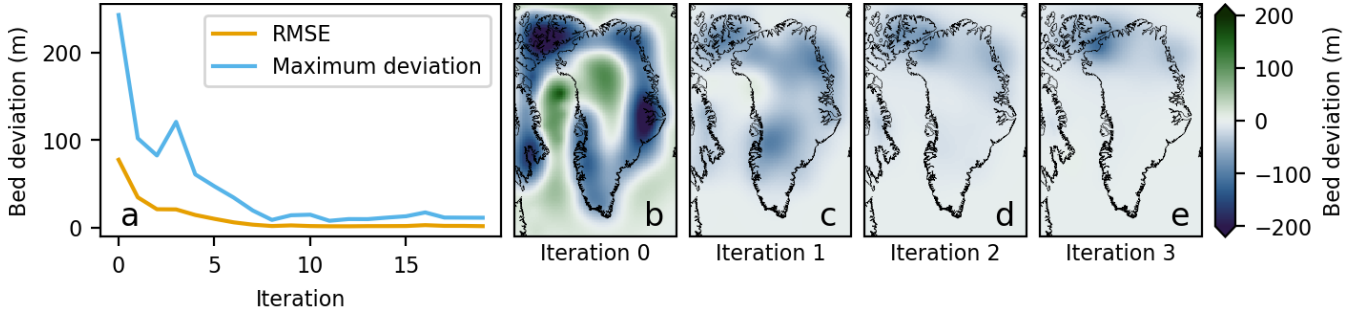


**Figure 3.** Iterative bedrock adjustment. (a) The modeled present-day bedrock elevation deviation compared to (Morlighem, 2022; Jakobsson et al., 2020; GEBCO Bathymetric Compilation Group, 2023). (b–e) shows the zeroth to the third iteration of the modeled present-day bedrock elevation deviation from observed.

170 change in our model setup. To effectively sample the parameter space, 841 parameters are drawn using the second-order orthogonal Latin Hypercube Sampling (LHS) design (Tang, 1993). This ensures that all pairs of parameters are sampled uniformly and reduces the risk of clustering. The parameters are sampled uniformly over the ranges specified in Table 1 which are based on the calibration by Aschwanden and Brinkerhoff (2022) and our previous model attempts.

For each of the four ice core sites, we calculate the likelihood, which is the probability of observing the ice-core-derived 175 elevation history given the modeled elevation change with model parameters  $\mathbf{m}$

$$\rho(\mathbf{h}_i^{\text{obs}}|\mathbf{m}) \propto \prod_j \exp\left(-\frac{(h_{i,j}(\mathbf{m}) - h_{i,j}^{\text{obs}})^2}{2\sigma_i^2\beta}\right), \quad (9)$$

where  $i$  denotes the ice core site and  $j$  is the time step of the ice core samples to which the modeled elevations are interpolated.  $\sigma_i$  are the uncertainties given by Vinther et al. (2009) which are constant in time. In this way, present-day and past surface elevations are given equal weight, and the likelihoods are thus not biased toward present-day configuration. Following Aschwanden and Brinkerhoff (2022), the parameter  $\beta = 100$  is introduced to account for the autocorrelation of the uncertainties such that estimated surface elevation has a standard deviation that is similar to the observed uncertainties  $\sigma_i$ . This effectively 180 reduces the number of degrees of freedom by a factor of 100 such that the decorrelation time becomes 2000 years.

Additionally, we calculate the combined likelihood of the ice-core-derived elevation changes to agree with the modeled elevation change for all sites. This likelihood is taken to be proportional to the product of the four individual likelihoods, 185 neglecting any spatial correlation between the drill sites:

$$\rho(\mathbf{h}^{\text{obs}}|\mathbf{m}) \propto \prod_{i=1}^4 \rho(\mathbf{h}_i^{\text{obs}}|\mathbf{m}). \quad (10)$$

The posterior joint probability density functions are then given by Bayes's theorem

$$\rho(\mathbf{m}|\mathbf{h}_i^{\text{obs}}) = \frac{\rho(\mathbf{h}_i^{\text{obs}}|\mathbf{m})}{\rho(\mathbf{h}_i^{\text{obs}})} \rho(\mathbf{m}), \quad (11)$$



Parameter	Description	Range	Estimates				
			Combined	CC	NGRIP	GRIP	Dye 3
<b>Atmosphere</b>							
$\Delta T$	Temperature reconstruction	1—5	1	1	4	2	3
$\psi_s$	PDD parameter for snow ( $\text{mm K}^{-1} \text{d}^{-1}$ )	5.7—8.9	$6.5 \pm 0.7$	$7.1 \pm 0.8$	$7 \pm 1$	$7.5 \pm 0.7$	$7.8 \pm 1.0$
$\psi_i$	PDD parameter for ice ( $\text{mm K}^{-1} \text{d}^{-1}$ )	7—10	$7.7 \pm 0.6$	$8.5 \pm 0.8$	$8.6 \pm 0.8$	$8.7 \pm 0.9$	$8.4 \pm 0.7$
$\Gamma$	Atmospheric lapse rate ( $\text{K km}^{-1}$ )	4—9	$5.4 \pm 0.7$	$7 \pm 1$	$6 \pm 1$	$6 \pm 1$	$6 \pm 1$
$\omega_{\downarrow}$	Precipitation scaling south of $60^\circ\text{N}$ ( $\% \text{K}^{-1}$ )	0—4.5	$2 \pm 1$				
$\omega_{\uparrow}$	Precipitation scaling north of $75^\circ\text{N}$ ( $\% \text{K}^{-1}$ )	0—9	$2 \pm 1$	$3 \pm 2$	$2 \pm 1$	$4 \pm 2$	$3 \pm 2$
<b>Ocean</b>							
$H_{cr}$	Threshold for thickness calving (m)	50—150	$96 \pm 17$	$87 \pm 25$	$97 \pm 30$	$112 \pm 30$	$106 \pm 30$
$\sigma_{max}$	Characteristic stress (MPa)	0.8—1.2	$0.92 \pm 0.09$	$1.03 \pm 0.10$	$1.0 \pm 0.1$	$1.0 \pm 0.1$	$1.0 \pm 0.1$
$\dot{m}_{\downarrow}$	Melt rate south of $71^\circ\text{N}$ ( $\text{m a}^{-1}$ )	300—500	$394 \pm 29$	$409 \pm 65$	$400 \pm 56$	$391 \pm 56$	$391 \pm 50$
$\dot{m}_{\uparrow}$	Melt rate north of $80^\circ\text{N}$ ( $\text{m a}^{-1}$ )	10—30	$20 \pm 6$	$19 \pm 6$	$21 \pm 6$	$19 \pm 6$	$19 \pm 5$
$\tau$	Ocean melt onset (ka)	4—8	$5.6 \pm 0.6$	$5.5 \pm 0.7$	$6 \pm 1$	$6 \pm 1$	$6 \pm 1$
$\Delta\tau$	Ocean melt set in time (ka)	0—2	$1.1 \pm 0.5$	$1.1 \pm 0.6$	$0.9 \pm 0.6$	$1.0 \pm 0.6$	$0.7 \pm 0.6$
<b>Dynamics</b>							
$n_{SSA}$	Creep exponent for the SSA (1)	3.2—3.4	$3.28 \pm 0.04$	$3.35 \pm 0.04$	$3.33 \pm 0.04$	$3.25 \pm 0.04$	$3.23 \pm 0.03$
$E_{SIA}$	Enhancement factor for the SIA (1)	2.5—3.3	$3.0 \pm 0.2$	$2.7 \pm 0.2$	$2.9 \pm 0.2$	$3.1 \pm 0.2$	$3.1 \pm 0.2$
$q$	Basal sliding power coefficient (1)	0.7—0.9	$0.82 \pm 0.05$	$0.79 \pm 0.05$	$0.81 \pm 0.06$	$0.80 \pm 0.06$	$0.83 \pm 0.06$
$\delta$	Effective pressure parameter (%)	1.5—2.5	$2.1 \pm 0.2$	$2.0 \pm 0.2$	$2.0 \pm 0.3$	$2.0 \pm 0.3$	$2.1 \pm 0.3$
$\phi_{min}$	Minimal till friction angle ( $^\circ$ )	5—10	$8 \pm 1$	$8 \pm 1$	$7 \pm 1$	$7 \pm 1$	$8 \pm 1$
$\phi_{max}$	Maximal till friction angle ( $^\circ$ )	40—45	$43 \pm 1$	$43 \pm 2$	$42 \pm 1$	$43 \pm 1$	$43 \pm 1$
$z_{min}$	Till friction cutoff elevation (m)	-600—300	$-421 \pm 60$	$-481 \pm 80$	$-443 \pm 84$	$-433 \pm 80$	$-447 \pm 77$
$z_{max}$	Till friction cutoff elevation (m)	0—500	$271 \pm 172$	$238 \pm 118$	$231 \pm 134$	$252 \pm 154$	$271 \pm 146$

**Table 1.** List of the 20 parameters that are varied in our ensemble of simulations. The temperature reconstruction is sampled discretely. The estimated parameter values are given as the mean plus minus the standard deviation of the posterior PDFs except for the temperature reconstruction, which is the mode of the posterior PDFs.

where the prior distribution  $\rho(\mathbf{m})$  is taken to be uniform within the intervals listed in Table 1. From the five posteriors, we get 190 five probability density functions of ice sheet evolution through the Holocene from which we estimate relevant observables listed in Table 2. Unless otherwise specified, all model results are given using the estimates from the combined posterior probability density function.

To evaluate the effectiveness of the sampling, we compute the effective sampling size (ESS) for each of our five posteriors:

$$ESS = \frac{(\sum_k \rho(\mathbf{h}_i^{\text{obs}} | \mathbf{m}_k))^2}{\sum_k \rho(\mathbf{h}_i^{\text{obs}} | \mathbf{m}_k)^2}, \quad (12)$$

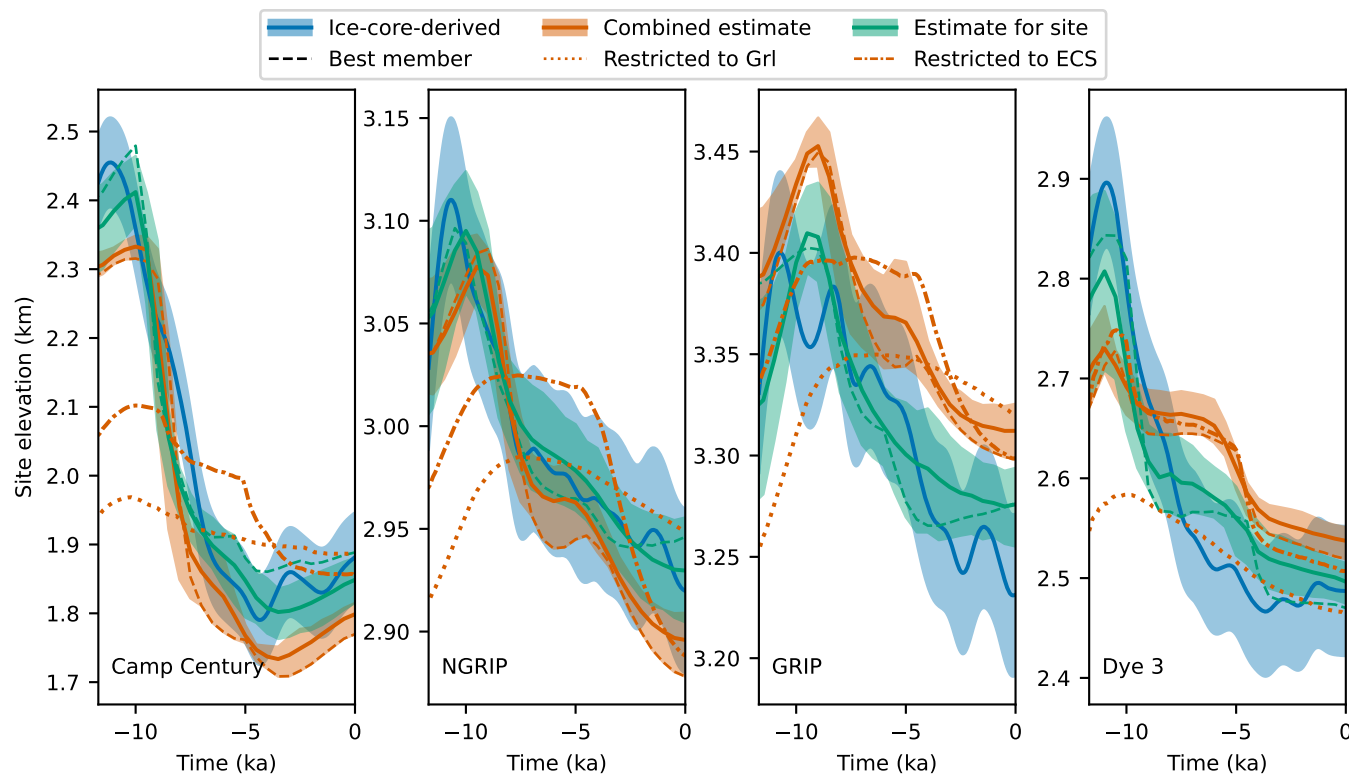


**Figure 4.** Observed and modeled surface elevation over the last 11.7 ka for the ice core sites, CC, NGRIP, GRIP, and Dye 3. The blue lines are the ice-core-derived surface elevations from Vinther et al. (2009), and the blue envelopes denote one standard deviation. The orange solid lines represent the combined estimate for all sites, while the green solid lines are the individual estimates for each ice core site. The shaded orange and green envelopes denote the estimated 16-84 quantile ranges. The dashed lines are the ensemble members with the highest likelihood for each site (green) and the highest combined likelihood (orange). The orange dotted and dash-dotted lines are simulations with the same parameters as the best ensemble member but restricted to ECS (dash-dotted) and the present-day land margin of the GrIS (dotted).

195 where  $k$  denotes the sample member.

## 5 Results

### 5.1 Surface elevation evolution

Figure 4 shows the modeled and the ice-core-derived surface elevations during the Holocene for the four ice-core sites. The individual estimates (green) for each site match the observed (blue) and reproduce the large thinning observed at CC and Dye 3 as well as the more moderate thinning in the interior at GRIP and NGRIP with RMSEs between 12 and 53.6 m. The combined estimated elevation (orange) is lower at CC and Dye 3 at the Holocene onset, while it is too high at GRIP compared to the individual estimates. Two simulations were restricted from advancing beyond the present-day GrIS coast, and the ECS mask

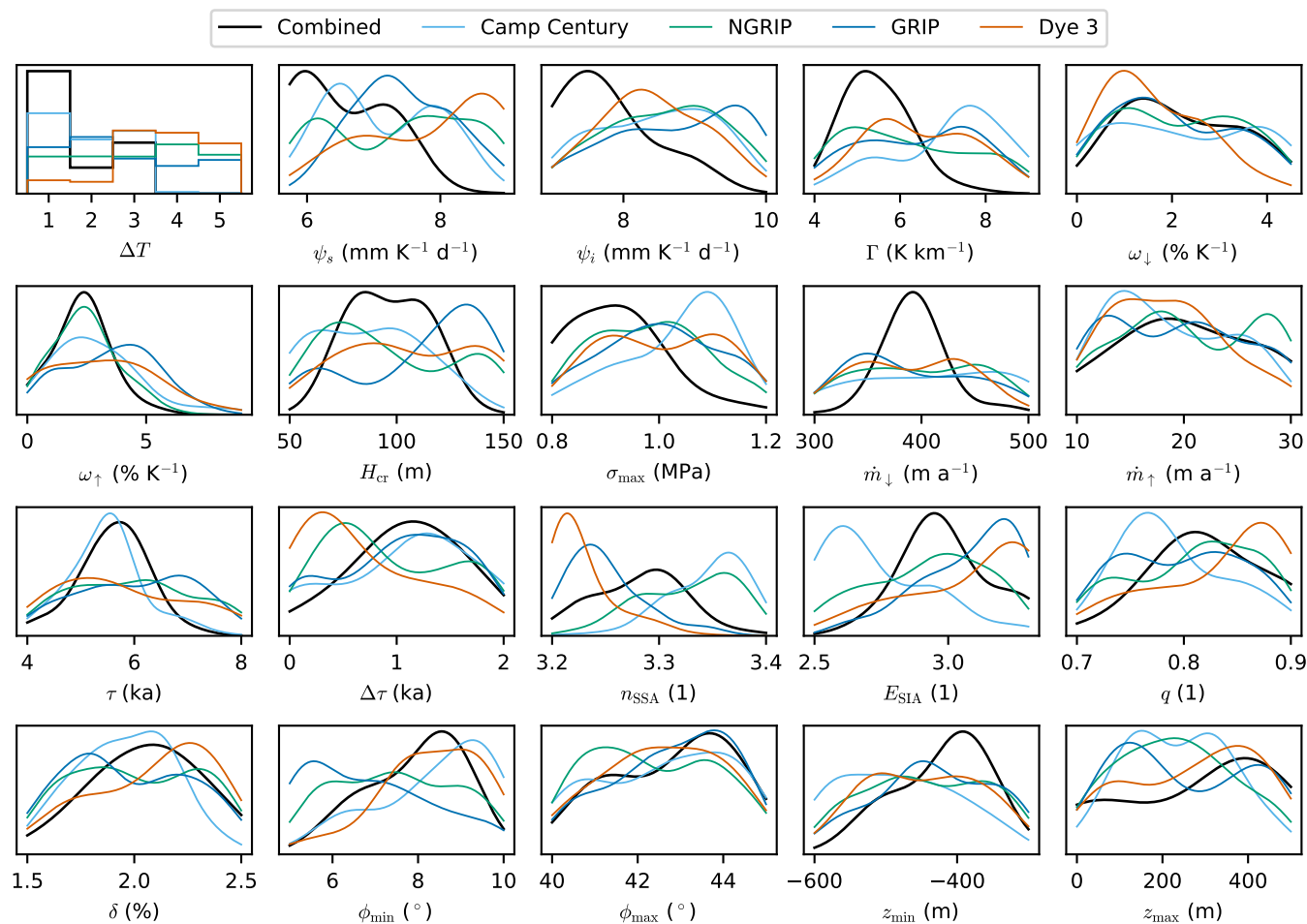


**Figure 5.** Kernel density estimates of the inferred marginal probability densities for the 20 model parameters that we varied. The units on the y-axes are the inverse of that of the x-axes.

was run with the same parameters as the ensemble member with the highest combined likelihood. The simulation restricted to the present-day GrIS coast could not reproduce the observed thinning at CC, NGRIP, and Dye 3, showing the importance of a dynamic grounding line. The simulation restricted to not advancing beyond the ECS performed better but also failed to reproduce the thinning at CC, showing the effect of including the IIS when modeling the GrIS Holocene history. The RMSEs to the four ice-core-derived elevation histories are listed in Table 2 for the five estimates.



## 5.2 Inferred parameters

The ice-core-derived surface elevation histories constrain the model parameters, and the marginal distributions for each of the  
210 five posteriors are shown in Fig. 5, and the estimated parameters are listed in Table 1. The inferred parameters are not equally  
well constrained and are constrained differently for each ice core site.

Notably, the estimated enhancement factor of the SIA,  $E_{SIA}$ , differs substantially between the sites. At CC, it is estimated to  
be  $2.7 \pm 0.2$ , while at GRIP, it is estimated to be  $3.1 \pm 0.2$ . The estimated creep exponent for the SSA,  $n_{SSA}$  also varies between  
the sites and has a higher estimate for CC and NGRIP than for GRIP and Dye 3.

215 Of the five different temperature reconstructions, the first temperature reconstruction from GRIP is the coldest through the  
Holocene and does not have a clear signal of the Holocene Thermal Maximum. It has the highest combined likelihood at 61%  
and the highest likelihood for CC at 40%, where the largest thinning is happening. The second temperature reconstruction from  
GRIP is more than a degree warmer in the early Holocene and does not perform as well as the first one. The fourth and fifth  
temperature reconstructions are the warmest through the Holocene and have near zero likelihood at CC, while the fourth is the  
220 most likely for NGRIP and Dye 3.

The northern accumulation parameter,  $\omega_{\uparrow}$ , is more constrained by the northern sites CC and NGRIP, where it has the most  
influence. Likewise, the southern accumulation parameter,  $\omega_{\downarrow}$ , is most constrained by Dye 3. Both parameters are estimated to  
be  $2 \pm 1\% \text{ K}^{-1}$  which is substantially lower than the default of  $7.3\% \text{ K}^{-1}$  introduced by Huybrechts (2002) resulting in less  
accumulation in the warm periods of the Holocene and more accumulation in the cold glacial where the ice sheet builds up.

225 The onset of sub-shelf ocean melt seems very well constrained by the CC surface elevation history and is estimated to happen  
at  $5.6 \pm 0.6 \text{ ka}$  before present. In the sections below, we will refer to the combined estimate (Fig. 5).

## 5.3 Modeled Holocene evolution

From the branch-off point at -20 ka until the onset of the Holocene (11.7 ka ago), the modeled ice sheet bridges the gap between  
Canada and Greenland over the Baffin Bay and the Nares Strait. Figure 6 shows the ice sheet configuration at -12 ka, -9 ka, and  
230 at present day, and Fig. 7 shows the volume and area evolution from the branch-off point until present day. At -12 ka, the ice  
sheet reaches its glacial maximum extent and is grounded to the continental shelf and through the Nares Strait. We will take  
this time step to represent the GrIS at the LGM in the following.

At the LGM, the GrIS has a modeled grounded area of  $2.96 \pm 0.03 \text{ km}^2$ , within the ECS, which is 49% or  $0.98 \pm 0.05 \times 10^6$   
 $\text{km}^2$  larger than the present-day modeled area and 13.2% larger than the LGM extent from Leger et al. (2024). Compared to  
235 the modeled present-day GrIS, the modeled grounded volume is  $6.6 \pm 0.4 \text{ m SLE}$  larger during the LGM. Additionally, the  
grounded volume above flotation is  $5.3 \pm 0.3 \text{ m SLE}$  larger, which contributed to the global mean sea level rise.

Outside the ECS the IIS and Laurentide Ice Sheet are cut off at the domain boundary with a Dirichlet boundary condition  
of zero thickness. This moves the ice divide at Baffin Island further to the east than if it had been connected to a complete  
Laurentide Ice Sheet. Together they have a grounded area of  $1.20 \pm 0.03 \times 10^6 \text{ km}^2$  and a grounded volume of  $5.0 \pm 0.2 \text{ m SLE}$ .



240 During the Holocene collapse of the IIS, the ice divide at the GrIS moves towards the west and the ice streams reorganize in northern Greenland as shown in Fig. 6.

Figure 8 shows the rate of change of grounded ice for the ensemble member with the highest combined likelihood for the seven basins of the GrIS. The GrIS rate of change becomes negative at -10.7 ka and peaks at -7.8 ka with a mass loss rate of 548 Gt a<sup>-1</sup> and after the onset of the sub-shelf melting at 4.95 ka with a mass loss rate of 511 Gt a<sup>-1</sup>. It continues to be  
245 negative for the rest of the Holocene except for a few times during the last 2 ka, where the average mass loss rate is 23.7 Gt a<sup>-1</sup>. The mass loss rates are averaged over 50 years.

#### 5.4 Present-day configuration

The modeled present-day extent of grounded ice deviates from the observed as shown in Fig. 9a. Most notably, it is larger at the Canadian Archipelago, while it fails to cover  $0.08 \pm 0.01$  km<sup>2</sup> and falsely covers  $0.19 \pm 0.01$  km<sup>2</sup> compared to the observed  
250 GrIS extent, including peripheral glaciers and neglecting ice thinner than 10 meters which is taken to be seasonal.

The modeled GrIS at present day has a grounded volume of  $9.1 \pm 0.1$  m SLE, which is 1.5 m SLE larger than the observed grounded volume, including peripheral glaciers (Morlighem, 2022). This can be explained by the ice thickness deviation at the margin of the GrIS shown in Fig. 9b.

Figure 10 shows the modeled surface speeds and the deviation compared to Solgaard and Kusk (2023). In the northwest, the  
255 modeled ice sheet is thinner than observed at the Humboldt Glacier, where the modeled surface speed is larger than observed. In the northeast, the model fails to capture the flow of the Northeast Greenland Ice Stream but has a faster-flowing ice stream north of it.

The modeled present-day uplift rates are shown in Fig. 11a together with GPS-derived GIA uplift rates from Schumacher et al. (2018). Figure 11b shows the difference between the modeled present-day bedrock topography and the observed. At  
260 present, the bedrock topography has a maximal deviation of 93 m in the area covered by the IIS and an RMSE of 27 m. Figure 11c shows the modeled bedrock topography uplift from the LGM at -12 ka to present day, which has a maximum of 509 m over the area covered by the IIS. At Agassiz, the bed uplift is  $345 \pm 9$  m while at Renland, it is  $168 \pm 9$  m, which is a little larger than the bed uplifts of 275 and 110 m respectively used by Vinther et al. (2009) for deriving the surface elevation histories.

## 6 Discussion

### 265 6.1 Inuitian ice bridge and the present-day response

To accurately model the ice-core-derived elevation history of the GrIS, we included the Canadian Arctic Archipelago in our domain. This inclusion supports the ice bridge connecting the GrIS and the IIS during the last glacial period. In our model, the IIS meets the GrIS at Nares Strait during the LGM. The ice then diverges into two streams: one flowing southwestward, similar to the Smith Ice Stream as suggested by England et al. (2006), and another flowing northeastward. The Smith Ice Stream

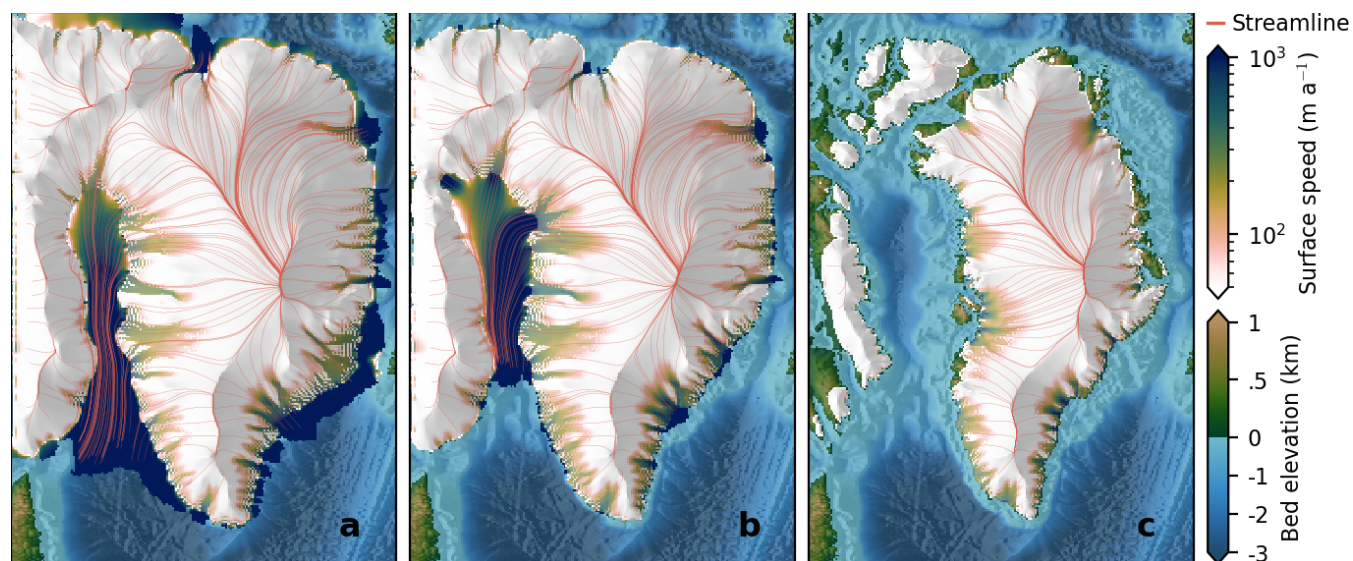


**Figure 6.** Time slices showing modeled surface speed, streamlines, bed topography, and ice shelf extent for the ensemble member with the highest combined likelihood at -12 ka (a), -9 ka (b), and present day (c).

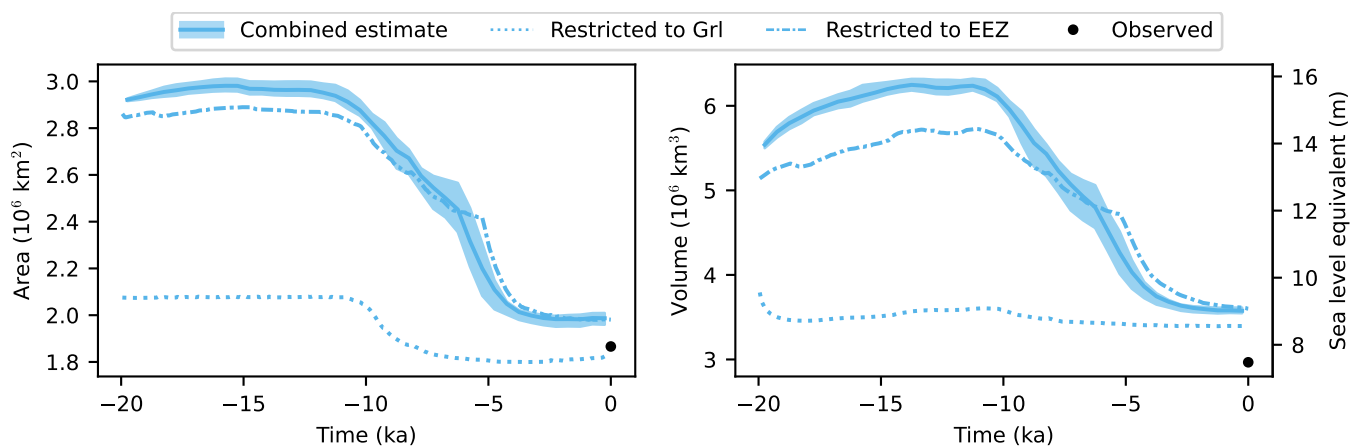


**Figure 7.** Modeled evolution of the GrIS grounded area (a) and volume (b). The shaded area denotes the estimated standard deviation.

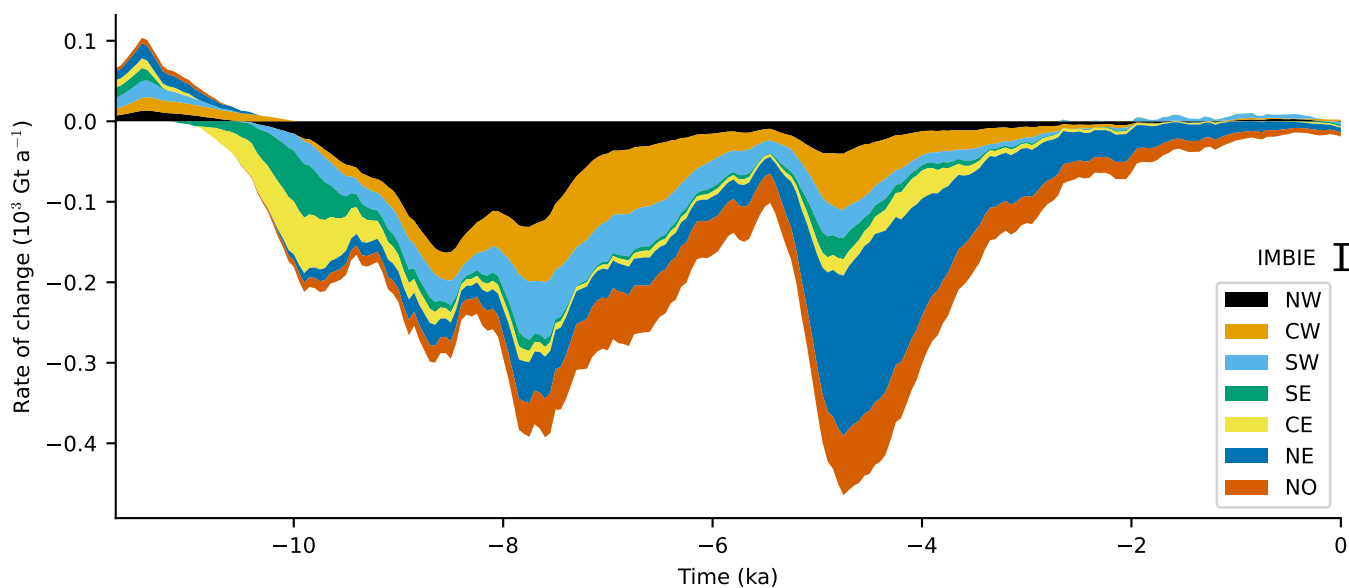


**Figure 8.** Rate of change of grounded ice by basin for the ensemble member with the highest likelihood. The mass change is smoothed using a running mean of 500 years, then divided into gain and loss, and then accumulated by basin. The 1992-2020 estimated mass loss rate from The IMBIE Team (2020) is shown for comparison.

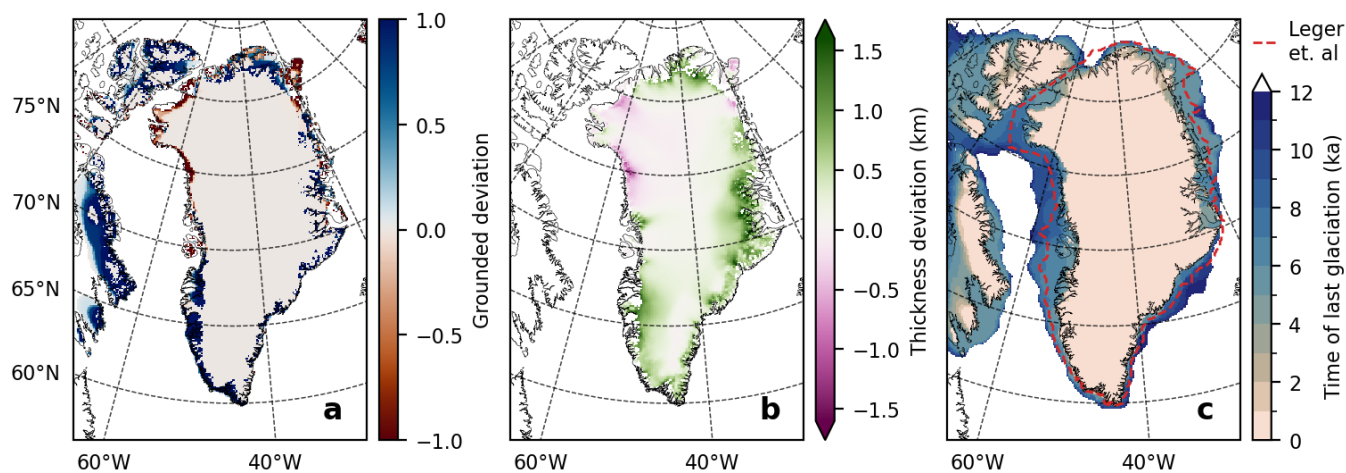


**Figure 9.** (a) Modeled present-day grounded extent deviation (modeled-obs) where one corresponds to grounded and zero corresponds to not grounded. (b) Modeled present-day thickness deviation from observed. (c) Isochrones showing the modeled time of the last glaciation together with the LGM extent from Leger et al. (2024).

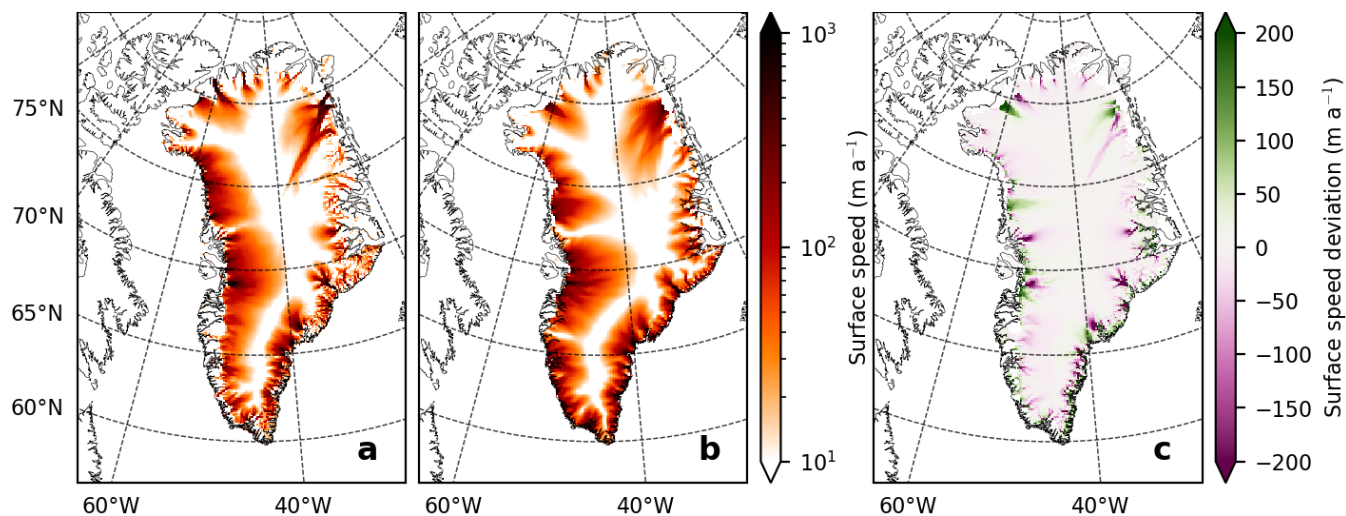


**Figure 10.** (a) Observed surface speeds over the GrIS from Solgaard et al. (2021). (b) Modeled present-day surface speeds. (c) Present-day surface speed deviation (mod-obs).

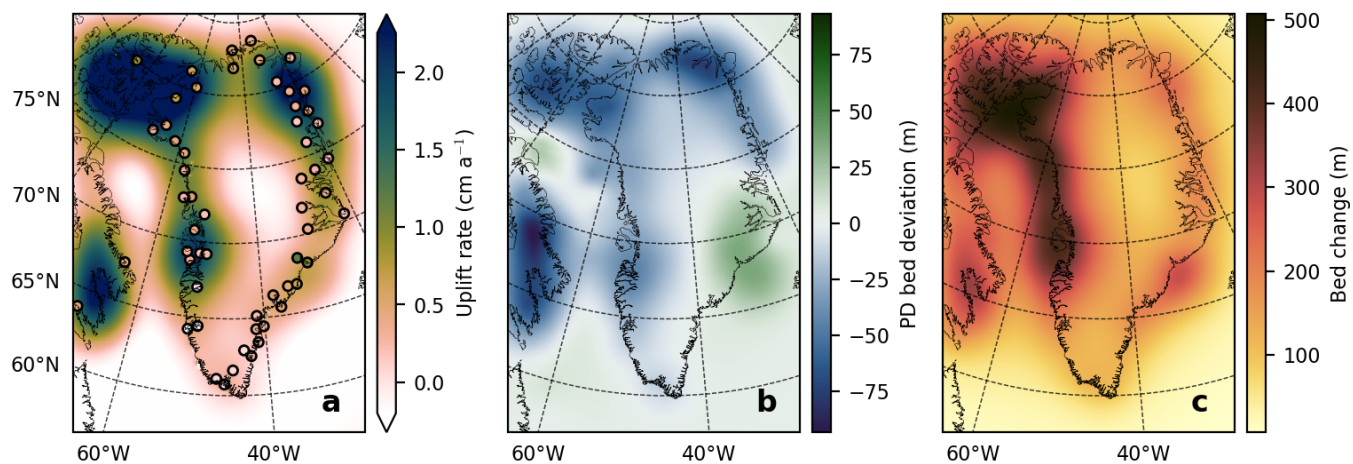


**Figure 11.** (a) Modeled present-day bedrock topography uplift rates and GPS-derived uplift rates from Schumacher et al. (2018). (b) Modeled present-day bedrock topography deviation from observed. (c) Modeled bed uplift between -12 ka and present-day.



Observable	Estimates						Restricted	
	Combined	CC	NGRIP	GRIP	Dye 3	Prior	Grl	ECS
Elevation history RMSE								
CC (m)	88.1	53.6	116.8	154.3	170.7	119	223.4	165.9
NGRIP (m)	26.8	44.9	12	69.8	69.4	34.9	67.8	49.9
GRIP (m)	58.6	123	86	27.2	29.5	62	64.5	59.5
Dye 3 (m)	99.1	153.4	116.4	87.2	55.4	106.1	123.5	88.5
Present-day configuration								
Grounded ice volume (m SLE)	9.0±0.1	9.5±0.3	9.1±0.3	8.7±0.3	8.7±0.2	9.0±0.4	8.55	9.08
Grounded area (10 <sup>6</sup> km <sup>2</sup> )	1.99±0.02	2.00±0.03	1.94±0.05	1.95±0.05	1.93±0.04	1.95±0.06	1.82	1.98
Falsely grounded (10 <sup>6</sup> km <sup>2</sup> )	0.19±0.01	0.21±0.02	0.17±0.03	0.18±0.03	0.17±0.03	0.18±0.04	0.07	0.19
Missing grounded (10 <sup>6</sup> km <sup>2</sup> )	0.08±0.01	0.08±0.01	0.11±0.02	0.11±0.02	0.12±0.02	0.10±0.02	0.13	0.08
Ice thickness RMSE <sup>†</sup> (m)	420.8	495.2	435.9	396.4	394.9	428	313.4	418.7
Bed topography RMSE (m)	27	42.2	19	18.5	17.5	20.2	58.3	58.3
Surface speed RMSE <sup>†</sup> (ma <sup>-1</sup> )	84.4	80.7	79.5	82.7	82	79.1	95.3	96.3
LGM configuration								
Grounded ice volume (m SLE)	15.7±0.3	16.0±0.7	15.8±0.5	15.1±0.6	15.8±0.7	15.3±0.9	9.03	14.31
Grounded area (10 <sup>6</sup> km <sup>2</sup> )	2.96±0.03	2.93±0.03	2.93±0.04	2.96±0.05	3.01±0.05	2.93±0.05	2.08	2.87
dvdt last 500 a (mm SLE ka <sup>-1</sup> )	-23±26	-31±27	-74±133	-52±106	-75±143	-60±112	-18.19	-70.81
Time of collapse (ka b2k)	4.9±0.5	4.9±0.7	6±1	6±1	5±1	6±1		
ESS	9.28	41.36	151.87	99.67	28.56	841.00		

**Table 2.** Estimates of key observables for the past and present of the GrIS, as well as observables for the simulations restricted to the present-day Greenland mask (Grl) and the ECS. All observables are calculated within the ECS mask and do not include Canada. <sup>†</sup> RMSEs are calculated within the present-day observed grounded mask.

270 discharges into the Baffin Bay, which, as proposed by Couette et al. (2022), is covered by an extensive ice sheet that provides buttressing for the western GrIS.

Figure 9c illustrates the modeled isochrones of areas last covered by grounded ice. The modeled collapse of the ice bridge in Nares Strait occurs at  $4.9 \pm 0.5$  ka before present, 0.7 ka after the onset of sub-shelf melting, and about 3 ka later than the findings by England et al. (2006). The ensemble members with earlier onsets of sub-shelf ocean melting become too thin at  
 275 Camp Century (CC) in the middle of the Holocene, while those with later onsets remain too thick at present. Although not the focus of this study, it may be possible to align the ice sheet evolution with both the elevation histories and the timing of the collapse by increasing the Holocene precipitation beyond present-day levels.

However, the importance of calibrating the GrIS evolution with paleo constraints is underscored when examining the mass change rates of the GrIS over the last 500 years. These rates range from a decrease of  $487 \text{ mm ka}^{-1}$  to an increase of  $105$   
 280  $\text{mm ka}^{-1}$  across the ensemble of simulations. Excluding the simulations that utilize the temperature reconstruction from



Gkinis et al. (2014), where the temperature anomaly peaks at 4.5 K during this period, we find that the remaining mass loss rates primarily depend on the timing of the onset of ocean forcing,  $\tau$ . This relationship exhibits a strong Pearson correlation coefficient of 0.8. Consequently, the estimated mass loss rate shifts from a prior of  $-12 \pm 40$  mm ka<sup>-1</sup> to a posterior of  $-23 \pm 26$  mm ka<sup>-1</sup>. This adjustment highlights the critical role of historical calibration in accurately modeling ice sheet dynamics.

## 285 6.2 Bedrock uplift

The present-day bedrock RMSE of the ensemble members varies between 11.9 and 70.9 m. This is less than the initial RMSE of 77.4 m before applying any bedrock adjustment but more than the RMSE of 1.47 m that was found for the 12th iteration of the bedrock adjustment scheme. This could partly be because the bedrock adjustment was done at a resolution of 20 km instead of the 10 km resolution of our ensemble, but the spread of the bedrock RMSE indicates that the modeled bedrock topography  
290 is very sensitive to the history of the ice load. One way to get a better agreement between the modeled present-day bedrock and the observed could be to make a few bedrock adjustment iterations for each ensemble member, although this would be computationally much more demanding. However, the reported error of Morlighem (2022) is up to 1000 m at the interior, where the data coverage is sparse, and the RMSE is 145 m over land, so getting a better agreement is of limited value due to the uncertainties in the bedrock topography.

295 The modeled uplift rates are larger than the GPS-derived GIA uplift rates from Schumacher et al. (2018) in most places. This could be explained by the modeled collapse happening too late and thus not providing enough time for the bed to relax or by the assumed viscosity of the upper mantle being too low. A higher viscosity would, in turn, make the past elevation change smaller, resulting in an earlier collapse.

The viscosity of the upper mantle was not varied in our ensemble, but the default of  $10^{21}$  Pa s from Lingle and Clark (1985)  
300 was used. Estimates of the viscosity range several orders of magnitude (Bagherbandi et al., 2022) and Albrecht et al. (2020) identifies a plausible range of viscosities to be  $10^{20} - 10^{22}$  Pa s for Antarctica. Varying the viscosity would change the bedrock topography history of the ensemble members even further, giving additional reason for adjusting the bedrock for each member individually.

## 6.3 Validity of elevation histories

305 The analysis made by Vinther et al. (2009) simplifies the relationships between the O-18 content of ice, temperature, and elevation changes. In particular, it does not account for the effect of an ice shelf over Baffin Bay or the influence of the IIS on the fractionation process along the moisture trajectory from the ocean to the ice core. Lecavalier et al. (2013) presented revised estimates of elevation histories, arguing that the bedrock history along the eastern coastline of Ellesmere Island should be used rather than at the Agassiz location itself while arguing that the IIS complicated the elevation correction before -8 ka.

310 Using the assumption that the elevation correction to the O-18 signal at the Agassiz ice cores should be taken from the shores, Lecavalier et al. (2017) presented revised temperature anomalies for the Agassiz ice core that, in turn, increased the ice-core-derived surface elevation at CC by 400 m at the Holocene onset.



The elevation histories presented by Vinther et al. (2009) have already been corrected for upstream effects due to ice flow. Ideally, the ice sheet model should be coupled to an atmosphere model that tracks the moisture from evaporation at the ocean  
315 to precipitation over the ice sheet and the fractionation of O-18. The modeled O-18 should then be compared directly to that of the observed at the time-dependent ice core site location.

The assumption that the thickness of the Renland ice cap does not change during the Holocene is not consistent with our model results, and we find that the Renland ice cap thins by  $399 \pm 56$  m from the Holocene onset to present day. We believe that this can be explained by the low resolution of the model resolution since the Renland ice cap is only  $1200 \text{ km}^2$  (Johnsen  
320 et al., 1992) and the model cannot capture the topography-sensitive steep descents that limit its lateral extent.

#### 6.4 Sampling technique

We used the second-order orthogonal LHS technique to effectively explore the 20 unknown model parameters critical to modeling the ice-core-derived surface elevation histories. This sampling strategy was chosen for its efficiency in covering a high-dimensional parameter space more uniformly compared to simple random sampling, thereby reducing errors in the  
325 estimation process. The effective sample size of the combined estimate is only 9.28, suggesting a significant concentration of weight among the samples, and the two most likely members contribute 42% to the estimates. One way to improve upon this could be to implement an adaptive sampling technique that concentrates the sampling density in the parts of the parameter space that have the highest contribution to the estimates, which we only did in an ad-hoc way, arriving at the sample ranges given in Table 1.

#### 330 6.5 Inferred parameters

Our analysis revealed that the estimated model parameters differed based on the ice core location used for their constraint. In particular, the enhancement factor for the SIA, the creep exponent for the SSA, the sliding exponent,  $q$ , and the climate history were constrained differently by the four ice core sites. The estimated parameters constrained by Camp Century (CC) in the northwest stand out with a lower enhancement factor for the SIA and a lower sliding exponent than elsewhere. The estimated  
335 parameters constrained by Dye 3 in the southwest stand out by a less sensitive southern precipitation scaling in the past and a smaller creep exponent for the SSA than elsewhere. The choice of temperature anomaly history also substantially impacted the modeled surface elevation histories. The temperature reconstructions without a Holocene Thermal Maximum were found to agree better with the ice-core-derived elevation history at CC, while the temperature reconstructions that did include a Holocene Thermal Maximum were found to agree well with the elevation histories at Dye 3 in the southeast. The ice sheet evolution in  
340 the Holocene is a complex result of many dynamical processes and climate forcings. While we have found a plausible range of ice sheet simulations constrained by the ice-core-derived surface elevation histories at four ice core sites, the difference in the individual estimates of model parameters suggests spatial differences that our analysis did not account for, e.g., in the basal geology and sliding, the lithosphere viscosity, or the accumulation rate in the early Holocene (e.g. Nielsen et al., 2018). The differences in the estimated ice flow parameters might also be explained by the poorly resolved outlet glaciers, which result  
345 in a lower ice flux. This is often compensated by increasing the enhancement factors. Notably, the Kangerlussuaq Gletscher



in eastern Greenland and Sermeq Kujalleq in western Greenland require a resolution of less than 3.6 km, as suggested by Aschwanden et al. (2016), to be properly resolved, which is not feasible for this study. Additionally, it is possible that the ice-core-derived surface elevation records do not provide sufficient constraints for all model parameters.

## 6.6 Climatic forcing

350 The atmospheric conditions and spatial patterns of temperature and precipitation during the glacial and the early Holocene were possibly quite different from that of present day. The Laurentide Ice Sheet is thought to have both shielded Ellesmere Island from precipitation and, at the same time, deflected the jet stream such that more moisture was transported north of the Laurentide Ice Sheet from the North Pacific Ocean to the Polar regions, making the amount of precipitation over Greenland uncertain (England et al., 2006). Furthermore, the ice shelf at Baffin Bay has likely affected the temperature and precipitation  
355 nonuniformly. A full coupling of ice sheets to the atmosphere and ocean would be needed to understand and investigate this effect in detail. However, the probability distributions for the five ice-core-derived temperature reconstructions do provide some insights into this. As mentioned above, the southern surface elevation history at Dye 3 was best fitted with a warm Holocene Thermal Maximum, while the northern CC site was best fitted with a constant Holocene climate. However, due to the bedrock elevation being depressed by up to 500 m in northern Greenland (Fig. 11c), the impact on temperature would be in the order of  
360 3-5°C (using the best fit atmospheric lapse rate for CC, see Fig. 5), similar to the impact proposed by other studies (e.g. Axford et al., 2021).

Lecavalier et al. (2017) also modeled the Holocene surface elevation change at CC. They used revised temperature anomalies from Agassiz that were 7 K warmer in the early Holocene than the present day, questioning the idea that a Greenland-wide temperature signal could accurately model the ice-core-derived elevation changes. They did, however, not include the buttressing  
365 effect of the IIS, which we find to be necessary. We also tried to use the temperature anomalies from Lecavalier et al. (2017) but found that although it did give an elevation change that was similar to the ice-core-derived, the modeled present-day elevation was far too low with the ice sheet retreating far inland in the northwest. However, our assumption of a uniform temperature change over the GrIS is a simplification, but further investigations are beyond the scope of this work.

## 6.7 Holocene evolution and ice mass loss

370 Overall, our simulations show that the deglaciation in Greenland occurred between around 10 ka and 3.5 ka, where the total area and volume of the GrIS dramatically decreased from its glacial maximum values to approximately the present-day volume and extent (Fig. 7). The minimum ice-covered area occurred approximately at -2 ka and slightly increased towards the present, while the ice volume has remained relatively constant over the last millennia. Our simulation shows no clear evidence of a minimum ice volume during the Holocene Thermal Maximum. It ends at the present day with a simulated area and volume  
375 that exceed the observed values by 5.9% and 20.5%, respectively (Fig. 7).

A previous study by Nielsen et al. (2018) showed that the evolution of the GrIS depends on the assumed climate history through the Holocene. Nielsen et al. (2018) found that the GrIS retreated to a smaller than present-day volume at around 8 ka ago when forced by temperature anomalies that contain the Holocene Thermal Maximum, but their simulations did not include



Canada in the domain, and thus initiated their simulation with a GrIS of similar size as at present day. In our simulations, we  
380 used the same climate forcing histories as in the study by Nielsen et al. (2018), but we do not find a similar minimum in our  
simulations for the ensemble members that include the Holocene Thermal Maximum, most likely because the GrIS is too far  
from equilibrium during the Holocene Thermal Maximum due to the large initial ice sheet. In fact, the simulations that best  
fit all surface elevation histories are those forced with the climate reconstruction history number 1 (see Fig. 5), which did not  
show any Holocene Thermal Maximum. For this climate reconstruction, our simulated Holocene ice volume follows a similar  
385 pattern as found in Nielsen et al. (2018).

The spatial pattern of mass loss rates from the GrIS has shifted significantly during the Holocene (Fig. 8). In the earliest part  
of the Holocene, the rate of mass change was slightly positive in all basins due to an increase in snow accumulation over the  
GrIS. During the first deglaciation phase between 10 and 5.5 ka ago, the mass loss rate was large in all basins, with the largest  
mass loss rate in the northwest basin, being about the same rate as all other basins combined. The central west basin also had  
390 significant mass loss rates, followed by the north and southwest basins. Towards 5.5 ka, the mass loss rates decreased towards  
zero, which is also seen in the volume record as a temporary stabilization. Between 5.5 ka and 3.5 ka, after the onset of the  
sub-shelf melt, a second phase in the deglaciation occurred, with a total higher mass loss rate than the first phase, and now  
dominated by high mass loss rates from the northeast basin and to a lesser extent from the north and central west basins. These  
two deglaciation phases are also seen in the total volume (Fig. 7b), with a kink around 5.5 ka ago separating the two phases.

395 Our simulated Holocene mass loss rates exceed the mass loss rates estimated in a previous study (Briner et al., 2020). Briner  
et al. (2020) simulated the Holocene evolution of the CW and SW basins and assumed that regions are representative of the  
entire GrIS. They found the maximal values of mass loss during the Holocene to be  $60 \text{ Gt a}^{-1}$  and that it would most likely be  
exceeded within this century with rates of mass loss of  $8.8$  to  $359 \text{ Gt a}^{-1}$  depending on the climate scenario which is less than  
our maximal Holocene rate of mass loss at  $548 \text{ Gt a}^{-1}$  for the ensemble member with the highest likelihood. Our results show  
400 that the spatial pattern of retreat has shifted geographically during the Holocene, and the mass loss rates from the GrIS basins  
have peaked thousands of years earlier in the northwest and west than in the northeast. We conclude that one basin cannot be  
representative of the entire GrIS, and thus, our results are not directly comparable to the results by Briner et al. (2020).

## 7 Conclusions

We considered an ensemble of ice sheet model simulations covering both Greenland and the Canadian Arctic Archipelago  
405 through the Holocene. In these simulations, we varied 20 key parameters to constrain the ice sheet evolution to ice-core-  
derived surface elevation histories at four ice-core sites in Greenland. We showed that the inclusion of Canada in the model  
domain and the ability of the ice sheet to advance beyond the present-day land margin are necessary for accurately modeling  
the ice-core-derived elevation history.

We found that during LGM, the Greenland ice sheet was connected to the IIS with an ice bridge over Nares Strait. Within  
410 the Extended Continental Shelf (ECS), the GrIS had an extent that was 49% larger than the present-day modeled area during



the LGM, and it was found to have contributed  $5.3 \pm 0.3$  m SLE to the global mean sea level from LGM to present day. The collapse of the ice bridge at Nares Strait was found to have occurred at  $4.9 \pm 0.5$  ka before the present.

We show that the present mass loss rate is a combined short-term response to the recent climate forcing and long-term dynamical response on millennia timescales due to the deglaciation history. Ignoring outliers with excessive temperature anomalies over the past half-millennium, we find that the mass loss rates over the last 500 years primarily depend on the timing of the onset of ocean forcing during the deglaciation. Bayesian inference modifies our understanding of the previous 500 years' mass loss from a prior estimation of  $12 \pm 40$  mm  $\text{ka}^{-1}$  to a posterior of  $23 \pm 26$  mm  $\text{ka}^{-1}$ , which is about 5% of the 1992-2020 estimated mass loss rate (The IMBIE Team, 2020) and 7% of the estimated 21st-century committed mass loss rate (Nias et al., 2023). This adjustment underscores the significance of historical calibration in accurately modeling ice sheet behavior and including its long-term response to past climatic changes.

While our study was able to model the ice-core derived surface elevation histories, the most probable ice sheet simulations did not match the timing of the collapse of the ice bridge found by England et al. (2006) or the timing of the retreat found by Leger et al. (2024). We propose that these geologically derived datings could be added as further constraints to the GrIS Holocene evolution in future simulations. This would help reveal limitations in the model and assess the sensitivity of model parameters. We also found that our modeled present-day uplift rates deviated from the GPS-derived uplift rates in northwest Greenland, which is further in line with the timing of our model collapse happening too late. In future studies, these deviations should be used to constrain the mantle viscosity in tandem with accurately determining the timing of the retreat. Overall, our results show that the present-day Greenland ice sheet still responds to the history of deglaciation. This long-term dynamical response is significant and should be included in studies of the present and future mass loss from the Greenland ice sheet.

*Code and data availability.* PISM is an open source software that can be downloaded from <https://github.com/pism/pism> (Bueler and Brown, 2009; Winkelmann et al., 2011). Surface elevation data from the four ice core locations are available upon request. The presented RACMO data are available upon request and without conditions from B. Noël (bnoel@uliege.be). Temperature reconstructions can be downloaded from [www.iceandclimate.nbi.ku.dk/data/](http://www.iceandclimate.nbi.ku.dk/data/).

*Video supplement.* A video showing the GrIS evolution through the Holocene for the most likely ensemble member can be found here

## 435 **Appendix A**

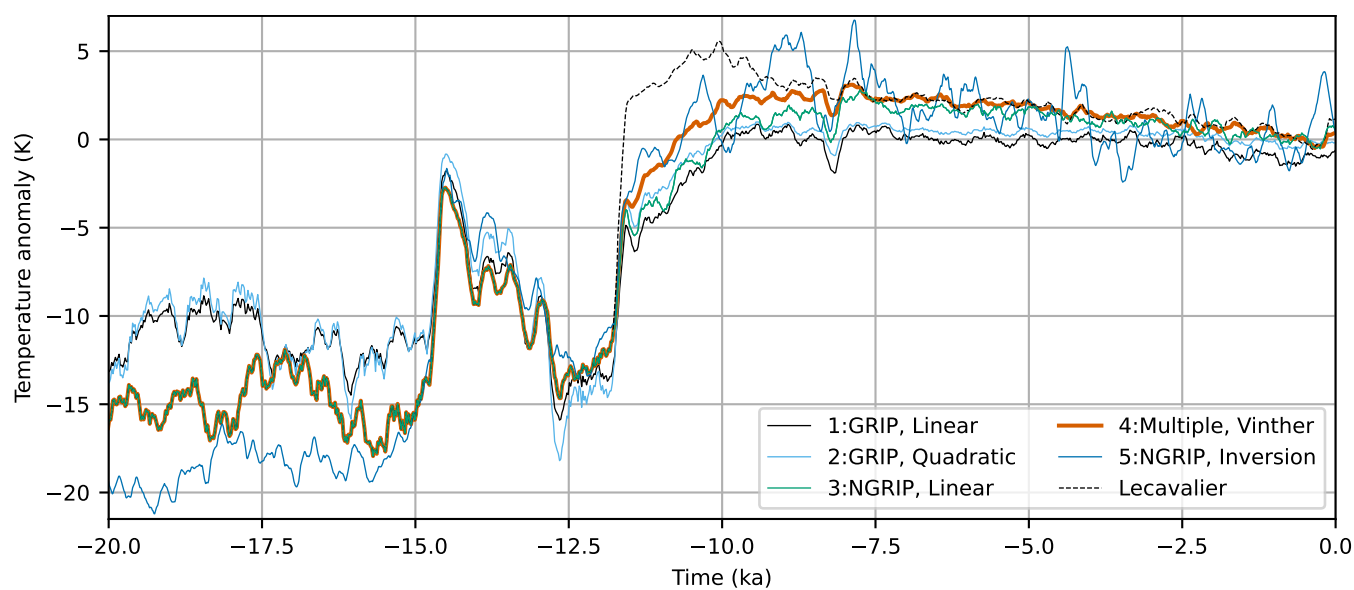


**Figure A1.** Paleoclimatic temperature anomalies derived from O-18 measurements at GRIP and NGRIP using linear transfer function (Huybrechts, 2002) and quadratic transfer function from Johnsen et al. (1995) and O-18 measurements at Renland and Agassiz (Vinther et al., 2009) and O-18 measurements at NGRIP using an inversion scheme (Gkinis et al., 2014).

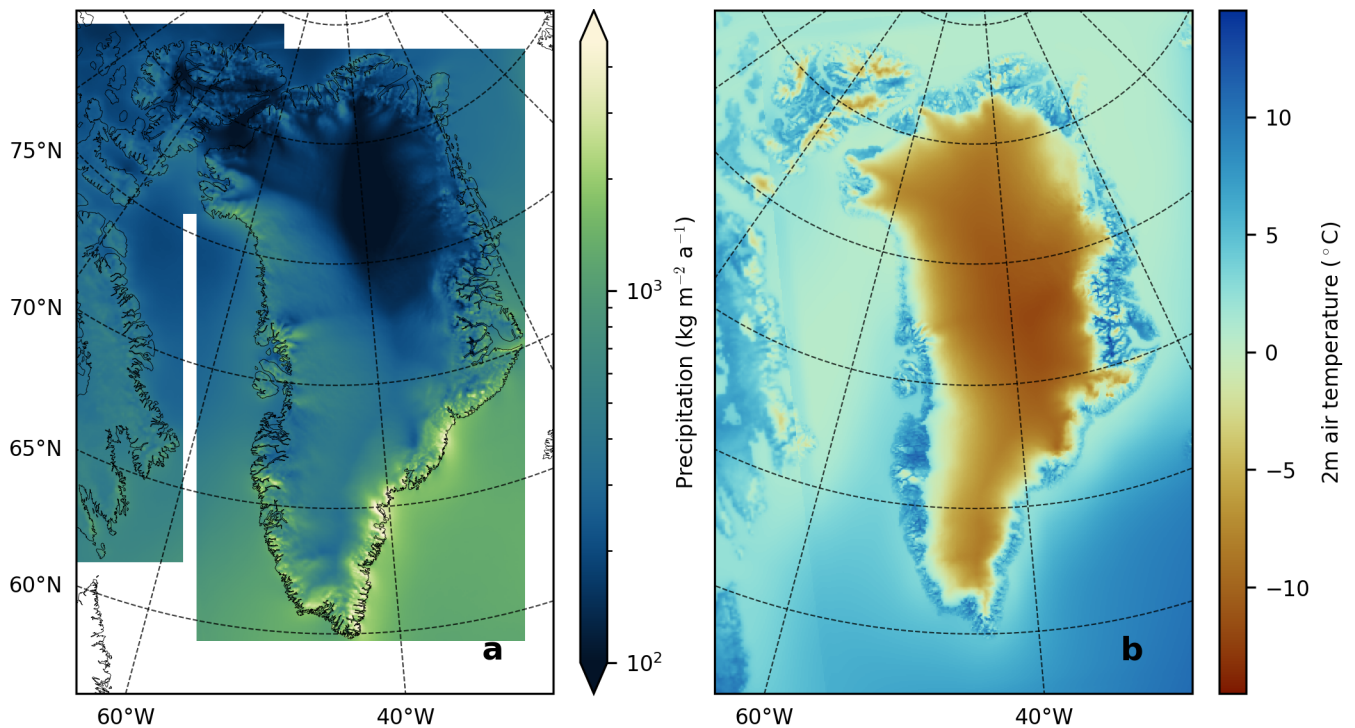


**Figure A2.** (a) Annual mean precipitation and (b) summer (June, July, and August) mean 2 m temperatures for our 30-year reference climatology.

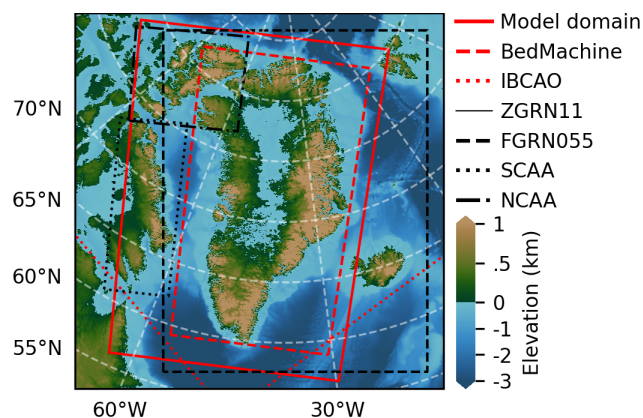


**Figure A3.** Overview of different domain boundaries used to patch together the 30-year reference climatology (ZGRN11, FGRN055, SCAA, NCAA) and the bedrock topography (BedMachine, IBCAO, GEBCO).

*Author contributions.* ML, CH, and AS designed the study. ML prepared the data, performed the model runs, and carried out the subsequent analysis. All authors discussed and improved the paper.

*Competing interests.* The authors declare that they have no conflict of interest.

*Acknowledgements.* ML was funded by the Independent Research Fund Denmark through the project GreenPlanning, grant no. 0217-440 00244B. CH, NR, and AG received funding from the Novo Nordisk Foundation, grant no. NNF23OC0081251, the Independent Research Fund Denmark (DFP), grant no. 2032-00364B, and the Villum Foundation, grant no. 23261. BN was funded by the Fonds de la Recherche Scientifique de Belgique (F.R.S.-FNRS). We would also like to thank Benoit Lecavalier for providing the temperature anomalies derived from the Agassiz ice core in Lecavalier et al. (2017).



## References

- 445 Adalgeirsdóttir, G., Aschwanden, A., Khroulev, C., Boberg, F., Mottram, R., Lucas-Picher, P., and Christensen, J.: Role of Model Initialization for Projections of 21st-Century Greenland Ice Sheet Mass Loss, *Journal of Glaciology*, 60, 782–794, <https://doi.org/10.3189/2014JoG13J202>, 2014.
- Albrecht, T., Winkelmann, R., and Levermann, A.: Glacial-Cycle Simulations of the Antarctic Ice Sheet with the Parallel Ice Sheet Model (PISM) – Part 2: Parameter Ensemble Analysis, *The Cryosphere*, 14, 633–656, <https://doi.org/10.5194/tc-14-633-2020>, 2020.
- 450 Andersen, K. K., Azuma, N., Barnola, J.-M., Bigler, M., Biscaye, P., Caillon, N., Chappellaz, J., Clausen, H. B., Dahl-Jensen, D., Fischer, H., Flückiger, J., Fritzsche, D., Fujii, Y., Goto-Azuma, K., Grønvold, K., Gundestrup, N. S., Hansson, M., Huber, C., Hvidberg, C. S., Johnsen, S. J., Jonsell, U., Jouzel, J., Kipfstuhl, S., Landais, A., Leuenberger, M., Lorrain, R., Masson-Delmotte, V., Miller, H., Motoyama, H., Narita, H., Popp, T., Rasmussen, S. O., Raynaud, D., Rothlisberger, R., Ruth, U., Samyn, D., Schwander, J., Shoji, H., Siggard-Andersen, M.-L., Steffensen, J. P., Stocker, T., Sveinbjörnsdóttir, A. E., Svensson, A., Takata, M., Tison, J.-L., Thorsteinsson, Th., Watanabe, O.,
- 455 Wilhelms, F., White, J. W. C., and North Greenland Ice Core Project members: High-Resolution Record of Northern Hemisphere Climate Extending into the Last Interglacial Period, *Nature*, 431, 147–151, <https://doi.org/10.1038/nature02805>, 2004.
- Aschwanden, A. and Brinkerhoff, D. J.: Calibrated Mass Loss Predictions for the Greenland Ice Sheet, *Geophysical Research Letters*, 49, e2022GL099058, <https://doi.org/10.1029/2022GL099058>, 2022.
- Aschwanden, A., Fahnestock, M. A., and Truffer, M.: Complex Greenland Outlet Glacier Flow Captured, *Nature Communications*, 7, 10 524, <https://doi.org/10.1038/ncomms10524>, 2016.
- 460 Aschwanden, A., Fahnestock, M. A., Truffer, M., Brinkerhoff, D. J., Hock, R., Khroulev, C., Mottram, R., and Khan, S. A.: Contribution of the Greenland Ice Sheet to Sea Level over the next Millennium, *Science Advances*, 5, eaav9396, <https://doi.org/10.1126/sciadv.aav9396>, 2019.
- Aschwanden, A., Bartholomäus, T. C., Brinkerhoff, D. J., and Truffer, M.: Brief Communication: A Roadmap towards Credible Projections
- 465 of Ice Sheet Contribution to Sea Level, *The Cryosphere*, 15, 5705–5715, <https://doi.org/10.5194/tc-15-5705-2021>, 2021.
- Axford, Y., De Vernal, A., and Osterberg, E. C.: Past Warmth and Its Impacts During the Holocene Thermal Maximum in Greenland, *Annual Review of Earth and Planetary Sciences*, 49, 279–307, <https://doi.org/10.1146/annurev-earth-081420-063858>, 2021.
- Bagherbandi, M., Amin, H., Wang, L., and Shirazian, M.: Mantle Viscosity Derived From Geoid and Different Land Uplift Data in Greenland, *Journal of Geophysical Research: Solid Earth*, 127, e2021JB023351, <https://doi.org/10.1029/2021JB023351>, 2022.
- 470 Bindschadler, R. A., Nowicki, S., Abe-Ouchi, A., Aschwanden, A., Choi, H., Fastook, J., Granzow, G., Greve, R., Gutowski, G., Herzfeld, U., Jackson, C., Johnson, J., Khroulev, C., Levermann, A., Lipscomb, W. H., Martin, M. A., Morlighem, M., Parizek, B. R., Pollard, D., Price, S. F., Ren, D., Saito, F., Sato, T., Seddik, H., Seroussi, H., Takahashi, K., Walker, R., and Wang, W. L.: Ice-Sheet Model Sensitivities to Environmental Forcing and Their Use in Projecting Future Sea Level (the SeaRISE Project), *Journal of Glaciology*, 59, 195–224, <https://doi.org/10.3189/2013JoG12J125>, 2013.
- 475 Braithwaite, R. J.: Calculation of Degree-Days for Glacier-Climate Research, *Zeitschrift für Gletscherkunde und Glazialgeologie*, 20/1984, 1–8, 1985.
- Briner, J. P., Cuzzone, J. K., Badgley, J. A., Young, N. E., Steig, E. J., Morlighem, M., Schlegel, N.-J., Hakim, G. J., Schaefer, J. M., Johnson, J. V., Lesnek, A. J., Thomas, E. K., Allan, E., Bennike, O., Cluett, A. A., Csatho, B., De Vernal, A., Downs, J., Larour, E., and Nowicki, S.: Rate of Mass Loss from the Greenland Ice Sheet Will Exceed Holocene Values This Century, *Nature*, 586, 70–74, <https://doi.org/10.1038/s41586-020-2742-6>, 2020.
- 480



- Bueler, E. and Brown, J.: Shallow Shelf Approximation as a “Sliding Law” in a Thermomechanically Coupled Ice Sheet Model, *Journal of Geophysical Research*, 114, F03 008, <https://doi.org/10.1029/2008JF001179>, 2009.
- Bueler, E. and van Pelt, W.: Mass-Conserving Subglacial Hydrology in the Parallel Ice Sheet Model Version 0.6, *Geoscientific Model Development*, 8, 1613–1635, <https://doi.org/10.5194/gmd-8-1613-2015>, 2015.
- 485 Bueler, E., Lingle, C. S., and Brown, J.: Fast Computation of a Viscoelastic Deformable Earth Model for Ice-Sheet Simulations, *Annals of Glaciology*, 46, 97–105, <https://doi.org/10.3189/172756407782871567>, 2007.
- Clark, P. U., He, F., Golledge, N. R., Mitrovica, J. X., Dutton, A., Hoffman, J. S., and Dendy, S.: Oceanic Forcing of Penultimate Deglacial and Last Interglacial Sea-Level Rise, *Nature*, 577, 660–664, <https://doi.org/10.1038/s41586-020-1931-7>, 2020.
- Couette, P.-O., Lajeunesse, P., Ghienne, J.-F., Dorschel, B., Gebhardt, C., Hebbeln, D., and Brouard, E.: Evidence for an Extensive Ice Shelf  
490 in Northern Baffin Bay during the Last Glacial Maximum, *Communications Earth & Environment*, 3, 225, <https://doi.org/10.1038/s43247-022-00559-7>, 2022.
- Dansgaard, W., Johnsen, S. J., Møller, J., and Langway, C. C.: One Thousand Centuries of Climatic Record from Camp Century on the Greenland Ice Sheet, *Science*, 166, 377–381, <https://doi.org/10.1126/science.166.3903.377>, 1969.
- England, J., Atkinson, N., Bednarski, J., Dyke, A., Hodgson, D., and Ó Cofaigh, C.: The Innuitian Ice Sheet: Configuration, Dynamics and  
495 Chronology, *Quaternary Science Reviews*, 25, 689–703, <https://doi.org/10.1016/j.quascirev.2005.08.007>, 2006.
- Eyring, V., Gillett, N., Achuta Rao, K., Barimalala, R., Barreiro Parrillo, M., Bellouin, N., Cassou, C., Durack, P., Kosaka, Y., McGregor, S., Min, S., Morgenstern, O., and Sun, Y.: Human Influence on the Climate System, in: *Climate Change 2021: The Physical Science Basis. Contribution of Working Group I to the Sixth Assessment Report of the Intergovernmental Panel on Climate Change*, edited by Masson-Delmotte, V., Zhai, P., Pirani, A., Connors, S., Péan, C., Berger, S., Caud, N., Chen, Y., Goldfarb, L., Gomis, M., Huang, M.,  
500 Leitzell, K., Lonnoy, E., Matthews, J., Maycock, T., Waterfield, T., Yelekçi, O., Yu, R., and Zhou, B., pp. 423–552, Cambridge University Press, Cambridge, United Kingdom and New York, NY, USA, <https://doi.org/10.1017/9781009157896.005>, 2021.
- Flanders Marine Institute (VLIZ), Belgium: Maritime Boundaries Geodatabase: Maritime Boundaries and Exclusive Economic Zones (200NM), Version 12, <https://doi.org/10.14284/632>, 2023.
- GEBCO Bathymetric Compilation Group: The GEBCO\_2023 Grid - a Continuous Terrain Model of the Global Oceans and Land.,  
505 <https://doi.org/10.5285/F98B053B-0CBC-6C23-E053-6C86ABC0AF7B>, 2023.
- Gkinis, V., Simonsen, S., Buchardt, S., White, J., and Vinther, B.: Water Isotope Diffusion Rates from the NorthGRIP Ice Core for the Last 16,000 Years – Glaciological and Paleoclimatic Implications, *Earth and Planetary Science Letters*, 405, 132–141, <https://doi.org/10.1016/j.epsl.2014.08.022>, 2014.
- Gladstone, R. M., Payne, A. J., and Cornford, S. L.: Parameterising the Grounding Line in Flow-Line Ice Sheet Models, *The Cryosphere*, 4,  
510 605–619, <https://doi.org/10.5194/tc-4-605-2010>, 2010.
- Gulev, S., Thorne, P., Ahn, J., Dentener, F., Domingues, C., Gerland, S., Gong, D., Kaufman, D., Nnamchi, H., Quaas, J., Rivera, J., Sathyendranath, S., Smith, S., Trewin, B., von Schuckmann, K., and Vose, R.: Changing State of the Climate System, in: *Climate Change 2021: The Physical Science Basis. Contribution of Working Group I to the Sixth Assessment Report of the Intergovernmental Panel on Climate Change*, edited by Masson-Delmotte, V., Zhai, P., Pirani, A., Connors, S., Péan, C., Berger, S., Caud, N., Chen, Y., Goldfarb, L., Gomis, M., Huang, M.,  
515 Leitzell, K., Lonnoy, E., Matthews, J., Maycock, T., Waterfield, T., Yelekçi, O., Yu, R., and Zhou, B., pp. 287–422, Cambridge University Press, Cambridge, United Kingdom and New York, NY, USA, <https://doi.org/10.1017/9781009157896.004>, 2021.
- Huybrechts, P.: Sea-Level Changes at the LGM from Ice-Dynamic Reconstructions of the Greenland and Antarctic Ice Sheets during the Glacial Cycles, *Quaternary Science Reviews*, 21, 203–231, [https://doi.org/10.1016/S0277-3791\(01\)00082-8](https://doi.org/10.1016/S0277-3791(01)00082-8), 2002.



- 520 Imbrie, J. D. and McIntyre, A.: SPECMAP Time Scale Developed by Imbrie et al., 1984 Based on Normalized Planktonic Records (Normalized O-18 vs Time, Specmap.017), <https://doi.org/10.1594/PANGAEA.441706>, 2006.
- Jakobsson, M., Mayer, L. A., Bringensparr, C., Castro, C. F., Mohammad, R., Johnson, P., Ketter, T., Accettella, D., Amblas, D., An, L., Arndt, J. E., Canals, M., Casamor, J. L., Chauché, N., Coakley, B., Danielson, S., Demarte, M., Dickson, M.-L., Dorschel, B., Dowdeswell, J. A., Dreutter, S., Fremand, A. C., Gallant, D., Hall, J. K., Hehemann, L., Hodnesdal, H., Hong, J., Ivaldi, R., Kane, E., Klauke, I., Krawczyk, D. W., Kristoffersen, Y., Kuipers, B. R., Millan, R., Masetti, G., Morlighem, M., Noormets, R., Prescott, M. M., Rebesco, M., Rignot, E., 525 Semiletov, I., Tate, A. J., Travaglini, P., Velicogna, I., Weatherall, P., Weinrebe, W., Willis, J. K., Wood, M., Zarayskaya, Y., Zhang, T., Zimmermann, M., and Zinglensen, K. B.: The International Bathymetric Chart of the Arctic Ocean Version 4.0, *Scientific Data*, 7, 176, <https://doi.org/10.1038/s41597-020-0520-9>, 2020.
- Johnsen, S. J., Clausen, H. B., Dansgaard, W., Gundestrup, N. S., Hansson, M., Jonsson, P., Steffensen, J. P., and Sveinbjörnsdóttir, A. E.: A "Deep" Ice Core from East Greenland, *Meddelelser om Grønland. Geoscience*, 29, 22 pp.–22 pp., 530 <https://doi.org/10.7146/moggeosci.v29i.140329>, 1992.
- Johnsen, S. J., Dahl-Jensen, D., Dansgaard, W., and Gundestrup, N.: Greenland Palaeotemperatures Derived from GRIP Bore Hole Temperature and Ice Core Isotope Profiles, *Tellus B: Chemical and Physical Meteorology*, 47, 624–629, <https://doi.org/10.3402/tellusb.v47i5.16077>, 1995.
- Lauritzen, M., Aðalgeirsdóttir, G., Rathmann, N., Grinsted, A., Noël, B., and Hvidberg, C. S.: The Influence of Inter-Annual Temperature 535 Variability on the Greenland Ice Sheet Volume, *Annals of Glaciology*, pp. 1–8, <https://doi.org/10.1017/aog.2023.53>, 2023.
- Lecavalier, B. S., Milne, G. A., Vinther, B. M., Fisher, D. A., Dyke, A. S., and Simpson, M. J.: Revised Estimates of Greenland Ice Sheet Thinning Histories Based on Ice-Core Records, *Quaternary Science Reviews*, 63, 73–82, <https://doi.org/10.1016/j.quascirev.2012.11.030>, 2013.
- Lecavalier, B. S., Fisher, D. A., Milne, G. A., Vinther, B. M., Tarasov, L., Huybrechts, P., Lacelle, D., Main, B., Zheng, J., Bourgeois, J., and 540 Dyke, A. S.: High Arctic Holocene Temperature Record from the Agassiz Ice Cap and Greenland Ice Sheet Evolution, *Proceedings of the National Academy of Sciences*, 114, 5952–5957, <https://doi.org/10.1073/pnas.1616287114>, 2017.
- Leger, T. P. M., Clark, C. D., Huynh, C., Jones, S., Ely, J. C., Bradley, S. L., Diemont, C., and Hughes, A. L. C.: A Greenland-wide Empirical Reconstruction of Paleo Ice Sheet Retreat Informed by Ice Extent Markers: PaleoGrIS Version 1.0, *Climate of the Past*, 20, 701–755, <https://doi.org/10.5194/cp-20-701-2024>, 2024.
- 545 Lingle, C. S. and Clark, J. A.: A Numerical Model of Interactions between a Marine Ice Sheet and the Solid Earth: Application to a West Antarctic Ice Stream, *Journal of Geophysical Research: Oceans*, 90, 1100–1114, <https://doi.org/10.1029/JC090iC01p01100>, 1985.
- Morlighem, M.: IceBridge BedMachine Greenland, Version 5, <https://doi.org/10.5067/GMEVBWFLWA7X>, 2022.
- Morlighem, M., Bondzio, J., Seroussi, H., Rignot, E., Larour, E., Humbert, A., and Rebuffi, S.: Modeling of Store Gletscher's Calving Dynamics, West Greenland, in Response to Ocean Thermal Forcing, *Geophysical Research Letters*, 43, 2659–2666, 550 <https://doi.org/10.1002/2016GL067695>, 2016.
- Mouginot, J. and Rignot, E.: Glacier Catchments/Basins for the Greenland Ice Sheet, <https://doi.org/10.7280/D1WT11>, 2019.
- Nias, I. J., Nowicki, S., Felikson, D., and Loomis, B.: Modeling the Greenland Ice Sheet's Committed Contribution to Sea Level During the 21st Century, *Journal of Geophysical Research: Earth Surface*, 128, e2022JF006914, <https://doi.org/10.1029/2022JF006914>, 2023.
- Nielsen, L. T., Aðalgeirsdóttir, Gu., Gkinis, V., Nuterman, R., and Hvidberg, C. S.: The Effect of a Holocene Climatic Optimum on the 555 Evolution of the Greenland Ice Sheet during the Last 10 Kyr, *Journal of Glaciology*, 64, 477–488, <https://doi.org/10.1017/jog.2018.40>, 2018.



- Noël, B., Van De Berg, W. J., Van Meijgaard, E., Kuipers Munneke, P., Van De Wal, R. S. W., and Van Den Broeke, M. R.: Evaluation of the Updated Regional Climate Model RACMO2.3: Summer Snowfall Impact on the Greenland Ice Sheet, *The Cryosphere*, 9, 1831–1844, <https://doi.org/10.5194/tc-9-1831-2015>, 2015.
- 560 Noël, B., van de Berg, W. J., Lhermitte, S., Wouters, B., Schaffer, N., and van den Broeke, M. R.: Six Decades of Glacial Mass Loss in the Canadian Arctic Archipelago, *Journal of Geophysical Research: Earth Surface*, 123, 1430–1449, <https://doi.org/10.1029/2017JF004304>, 2018.
- Noël, B., Van De Berg, W. J., Lhermitte, S., and Van Den Broeke, M. R.: Rapid Ablation Zone Expansion Amplifies North Greenland Mass Loss, *Science Advances*, 5, eaaw0123, <https://doi.org/10.1126/sciadv.aaw0123>, 2019.
- 565 Nowicki, S., Goelzer, H., Seroussi, H., Payne, A. J., Lipscomb, W. H., Abe-Ouchi, A., Agosta, C., Alexander, P., Asay-Davis, X. S., Barthel, A., Bracegirdle, T. J., Cullather, R., Felikson, D., Fettweis, X., Gregory, J. M., Hattermann, T., Jourdain, N. C., Kuipers Munneke, P., Larour, E., Little, C. M., Morlighem, M., Nias, I., Shepherd, A., Simon, E., Slater, D., Smith, R. S., Straneo, F., Trusel, L. D., Van Den Broeke, M. R., and Van De Wal, R.: Experimental Protocol for Sea Level Projections from ISMIP6 Stand-Alone Ice Sheet Models, *The Cryosphere*, 14, 2331–2368, <https://doi.org/10.5194/tc-14-2331-2020>, 2020.
- 570 Rasmussen, S. O., Andersen, K. K., Svensson, A. M., Steffensen, J. P., Vinther, B. M., Clausen, H. B., Siggaard-Andersen, M.-L., Johnsen, S. J., Larsen, L. B., Dahl-Jensen, D., Bigler, M., Röthlisberger, R., Fischer, H., Goto-Azuma, K., Hansson, M. E., and Ruth, U.: A New Greenland Ice Core Chronology for the Last Glacial Termination, *Journal of Geophysical Research: Atmospheres*, 111, <https://doi.org/10.1029/2005JD006079>, 2006.
- RGI Consortium: Randolph Glacier Inventory - A Dataset of Global Glacier Outlines, Version 7, <https://doi.org/10.5067/F6JMOVY5NAVZ>, 2023.
- 575 Schumacher, M., King, M. A., Rougier, J., Sha, Z., Khan, S. A., and Bamber, J. L.: A New Global GPS Data Set for Testing and Improving Modelled GIA Uplift Rates, *Geophysical Journal International*, 214, 2164–2176, <https://doi.org/10.1093/gji/ggy235>, 2018.
- Shapiro, N.: Inferring Surface Heat Flux Distributions Guided by a Global Seismic Model: Particular Application to Antarctica, *Earth and Planetary Science Letters*, 223, 213–224, <https://doi.org/10.1016/j.epsl.2004.04.011>, 2004.
- 580 Solgaard, A., Kusk, A., Merryman Boncori, J. P., Dall, J., Mankoff, K. D., Ahlstrøm, A. P., Andersen, S. B., Citterio, M., Karlsson, N. B., Kjeldsen, K. K., Korsgaard, N. J., Larsen, S. H., and Fausto, R. S.: Greenland Ice Velocity Maps from the PROMICE Project, *Earth System Science Data*, 13, 3491–3512, <https://doi.org/10.5194/essd-13-3491-2021>, 2021.
- Solgaard, A. M. and Kusk, A.: Greenland Ice Velocity from Sentinel-1 Edition 3, <https://doi.org/10.22008/FK2/ZEGVXU>, 2023.
- Tang, B.: Orthogonal Array-Based Latin Hypercubes, *Journal of the American Statistical Association*, 88, 1392–1397, <https://doi.org/10.2307/2291282>, 1993.
- 585 The IMBIE Team: Mass Balance of the Greenland Ice Sheet from 1992 to 2018, *Nature*, 579, 233–239, <https://doi.org/10.1038/s41586-019-1855-2>, 2020.
- Vinther, B. M., Buchardt, S. L., Clausen, H. B., Dahl-Jensen, D., Johnsen, S. J., Fisher, D. A., Koerner, R. M., Raynaud, D., Lipenkov, V., Andersen, K. K., Blunier, T., Rasmussen, S. O., Steffensen, J. P., and Svensson, A. M.: Holocene Thinning of the Greenland Ice Sheet, *Nature*, 461, 385–388, <https://doi.org/10.1038/nature08355>, 2009.
- 590 Winkelmann, R., Martin, M. A., Haseloff, M., Albrecht, T., Bueller, E., Khroulev, C., and Levermann, A.: The Potsdam Parallel Ice Sheet Model (PISM-PIK) – Part 1: Model Description, *The Cryosphere*, 5, 715–726, <https://doi.org/10.5194/tc-5-715-2011>, 2011.